

BAYESIAN MIXED-EFFECTS MODELS FOR MULTILEVEL TWO-WAY FUNCTIONAL DATA: APPLICATIONS TO EEG EXPERIMENTS

BY XIAOMENG JU^{1,a}, THADDEUS TARPEY^{1,b} AND HYUNG G PARK^{1,c}

¹*Division of Biostatistics, Department of Population Health, New York University*, ^ajux01@nyu.edu;
^bThaddeus.Tarpey@nyulangone.org; ^cparkh15@nyu.edu

In multi-condition EEG experiments, brain activity is recorded as subjects perform various tasks or are exposed to different stimuli. The recorded signals are commonly transformed into time-frequency representations, which often display smooth variations across time and frequency dimensions. These representations are naturally structured as two-way functional data, with experimental conditions nested within subjects. Existing analytical methods fail to jointly account for the data’s multilevel structure, functional nature, and dependence on subject-level covariates. To address these limitations, we propose a Bayesian mixed-effects model for two-way functional data that incorporates covariate-dependent fixed effects at the condition level and multilevel random effects. For enhanced model interpretability and parsimony, we introduce a novel covariate-dependent CANDECOMP/PARAFAC (CP) decomposition for the fixed effects, with marginally interpretable time and frequency patterns. We further propose a sparsity-inducing prior for CP rank selection and an efficient algorithm for posterior sampling. The proposed method is evaluated through extensive simulations and applied to EEG data collected to investigate the effects of alcoholism on cognitive processing in response to visual stimuli. Our analysis reveals distinct patterns of time-frequency activity associated with alcoholism, offering new insights into the neural processing differences between subject groups and experimental conditions.

1. Introduction. Electroencephalography (EEG) is a non-invasive neuroimaging procedure that records electrical voltage on the scalp with high temporal resolution. Many EEG studies adopt a multi-condition design, where each subject (i.e., participant) performs different tasks or is exposed to various stimuli, each of which defines an experimental condition (Malik and Amin, 2017). EEG signals are recorded for each condition per subject, resulting in a multilevel data structure. These signals are commonly transformed into the time-frequency domain to analyze dynamic neural oscillatory patterns (Morales and Bowers, 2022), which typically vary smoothly over the time and frequency domains and can be effectively modeled as two-way functional data. In many studies, EEG data are supplemented by subject-level covariates, such as demographic variables or clinical diagnoses, which may influence neural responses to experimental conditions. The goal is to uncover how brain responses vary by condition as a function of covariates in the time-frequency domain, while separating condition-specific effects from subject-level variability. This task presents statistical challenges in multi-condition EEG experiments due to the data’s multilevel structure, two-way functional nature, and dependence on auxiliary covariates. While existing methods have addressed one or two of these challenges, there lacks a unified solution that tackles all three challenges effectively.

A variety of methods have been developed to analyze multi-condition EEG data, however, many do not fully account for the multilevel structure inherent in such datasets. Some approaches jointly model multiple conditions for a single subject, allowing information sharing

Keywords and phrases: functional data, Bayesian, mixed-effect models, neuroimaging.

across conditions (Gramfort and Kowalski, 2009; Wu et al., 2014), but they are not suited for multi-subject studies where borrowing information across individuals is beneficial. For multi-subject studies, methods based on tensor decomposition (Cong et al., 2015) and Gaussian processes (Marquand et al., 2014) have been explored to capture intra-subject correlations. However, these methods do not explicitly separate population-level condition effects from subject-specific effects reflecting individual variability, and are unable to accommodate auxiliary covariates or functional features.

Mixed-effects models provide an interpretable and flexible framework for EEG analysis, naturally accommodating multilevel data structures in which measurements are nested within subjects across experimental conditions, repeated trials, or brain regions. Most developments of mixed-effects models in EEG studies consider scalar or vector features extracted from raw signals (Spinnato et al., 2015; Riha et al., 2020; Meinardi et al., 2024; Palma et al., 2024). More recently, mixed-effects models have been extended to functional EEG data to capture continuous changes of signals over time. These extensions include parametric models for univariate functional outcomes (Dong et al., 2024), Gaussian processes for multivariate functional responses with hierarchical mean structures (Li et al., 2020), and multilevel functional principal component analysis (FPCA) for multivariate functions (Campos et al., 2022; Zhang et al., 2023). Among these, Dong et al. (2024) and Li et al. (2020) incorporate covariate information into the fixed effects, whereas Campos et al. (2022) and Zhang et al. (2023) focus on covariance decomposition without covariate modeling.

Beyond EEG applications, a wide range of statistical methods have been proposed to extract low-dimensional and interpretable features from multivariate or higher-order functional data. These include singular value decomposition (SVD) for multivariate functions (Alam, Staicu and Shi, 2024) and tensors with one functional mode (Han, Shi and Zhang, 2024), CANDECOMP/PARAFAC (CP) decomposition for tensors with one functional mode (Sort, Brusquet and Tenenhaus, 2024), FPCA for multi-way functional data (Allen, 2013; Chen and Jiang, 2017) and multivariate functional data (Happ and Greven, 2018), and latent factor Gaussian processes for two-way functional data (Shamshoian et al., 2022). While these methods are powerful for dimension reduction, they do not account for study designs with multilevel data structures.

Existing methods for multilevel functional data are limited to univariate or multivariate functions, and are not directly applicable to two-way functional observations. These include multilevel FPCA approaches (Di et al., 2009; Greven et al., 2011; Zipunnikov et al., 2014; Cui et al., 2023), (generalized) linear mixed-effects models (Guo, 2002; Morris et al., 2003; Morris and Carroll, 2006; Cederbaum et al., 2016; Cui et al., 2022; Sun and Kowal, 2025), and (generalized) additive mixed-effects models (Scheipl, Staicu and Greven, 2015; Scheipl, Gertheiss and Greven, 2016; Volkmann et al., 2023). Other related methods include linear mixed-effects models for matrix-valued data (Huang et al., 2019) and CP decomposition for multilevel tensor data (Tang, Bi and Qu, 2020). While these methods can model smooth variation over the functional domains when applied to two-way functional data, they become computationally expensive for dense functional observations.

To address the limitations of existing approaches, we propose a novel Bayesian mixed-effects model for two-way functional data, motivated by time-frequency analysis in multi-condition EEG experiments. To our knowledge, this is the first approach to jointly address three key challenges: (i) the multilevel data structure from multi-subject, multi-condition designs, (ii) the two-way functional nature of time-frequency features, and (iii) the incorporation of subject-level covariates. The model builds on a covariate-assisted CANDECOMP/PARAFAC (CP) decomposition of the fixed effects, with a sparsity-inducing prior for automatic rank selection. Random effects are specified at two levels to capture individual

variability shared across conditions and specific to each condition. For scalable posterior inference, we generalized the efficient posterior sampling algorithm of [Sun and Kowal \(2025\)](#) from univariate to two-way functional mixed-effects models.

A key advantage of our approach is its interpretability. The proposed approach identifies two-way functional patterns in the fixed effects shared across subjects and conditions, which can be decomposed into marginal functional components along the time and frequency dimensions. In the EEG context, these marginals often carry meaningful neurophysiological interpretations, such as temporal dynamics and frequency-specific activation of neural responses. Covariates influence how these patterns are modulated across conditions, allowing us to evaluate the impact of subject-level covariates on neural responses and to make predictions under covariate shifts. This covariate-assisted formulation of the fixed effects can be viewed as an extension of the supervised CP decomposition ([Lock and Li, 2018](#)) to functional data. In addition, our model supports inference on random effects that capture both shared and condition-specific variation at the subject level. This provides a more complete understanding of individual differences in neural responses, beyond those that can be explained by the observed covariates.

The remainder of the paper is organized as follows. Section 2 introduces the proposed mixed-effects model and describes an efficient Markov chain Monte Carlo (MCMC) algorithm for posterior inference with rank selection. Section 3 evaluates the proposed method through simulation studies, comparing its performance to existing alternatives. Section 4 demonstrates the approach using EEG data from an alcoholism study, and Section 5 discusses the key findings and contributions.

2. Methodology. We consider data collected from n subjects across J experimental conditions. For each subject with subject-level covariates $\mathbf{x}_i \in \mathbb{R}^p$ ($i = 1, \dots, n$), we observe two-way functions $\mathcal{Y}_{i,j}(\mathbf{x}_i) : \mathcal{I}_1 \times \mathcal{I}_2 \rightarrow \mathbb{R}$, under conditions $j \in \mathcal{J}_i \subseteq \{1, \dots, J\}$, where $\bigcup_{i=1}^n \mathcal{J}_i = \{1, \dots, J\}$. Let us denote noisy realizations of $\mathcal{Y}_{i,j}$ by $Y_{i,j}$. We model $Y_{i,j}(t, f)$ in a mixed-effects framework:

$$(1) \quad Y_{i,j}(t, f) = \mathcal{A}_j(\mathbf{x}_i)(t, f) + \mathcal{B}_i(t, f) + \mathcal{C}_{i,j}(t, f) + \mathcal{E}_{i,j}(t, f), \quad t \in \mathcal{I}_1, f \in \mathcal{I}_2,$$

where $\mathcal{A}_j(\mathbf{x}_i)(t, f)$ denotes the covariate-dependent fixed effect for condition j , $\mathcal{B}_i(t, f)$ captures the random effect shared across conditions for subject i , $\mathcal{C}_{i,j}(t, f)$ represents the condition-specific random effect for subject i , and $\mathcal{E}_{i,j}(t, f)$ accounts for the random noise. In the absence of covariates, model (1) reduces to a functional analysis of variance (FANOVA) ([Ramsay and Silverman, 2005](#)) model for two-way functional data, where the fixed-effect $\mathcal{A}_j(t, f)$ represents the population mean surface corresponding to experimental condition j .

In model (1), we assume that the fixed and random effects ($\mathcal{A}_j(\mathbf{x}_i)$, \mathcal{B}_i , and $\mathcal{C}_{i,j}$) are smooth functions defined over the two-way domain $\mathcal{I}_1 \times \mathcal{I}_2$. These functions are estimated from discrete observations of $Y_{i,j}(t, f)$ on a grid $\mathbf{t} \times \mathbf{f}$, where $\mathbf{t} = (t_1, \dots, t_T)$ and $\mathbf{f} = (f_1, \dots, f_F)$. In the EEG setting, these observations correspond to measurements of neural oscillations (e.g., oscillatory power) evaluated at T time points and F frequency points. The noise term $\mathcal{E}_{i,j}(t, f)$ is assumed to have zero mean and is independent across (t, f) and from random effects (\mathcal{B}_i and $\mathcal{C}_{i,j}$). We allow for subject-level missing conditions—that is, not all conditions need to be observed for every subject, as is often the case in practice.

2.1. Tensor product basis representation. We represent the two-way functions $\mathcal{A}_j(\mathbf{x})$, \mathcal{B}_i and $\mathcal{C}_{i,j}$ in (1) using a tensor product basis $\Omega(t, f) = \boldsymbol{\psi}(f) \otimes \boldsymbol{\phi}(t) \in \mathbb{R}^K$, constructed as the Kronecker product of marginal basis functions $\boldsymbol{\phi}(t) = (\phi_1(t), \dots, \phi_{K_T}(t))^T \in \mathbb{R}^{K_T}$ (for the time domain) and $\boldsymbol{\psi}(f) = (\psi_1(f), \dots, \psi_{K_F}(f))^T \in \mathbb{R}^{K_F}$ (for the frequency domain), where $K = K_T K_F$. Specifically, the fixed and random effects are expressed as:

$$(2) \quad \mathcal{A}_j(\mathbf{x})(t, f) = \mathbf{a}_j(\mathbf{x})^T \Omega(t, f), \quad \mathcal{B}_i(t, f) = \mathbf{b}_i^T \Omega(t, f), \quad \mathcal{C}_{i,j}(t, f) = \mathbf{c}_{i,j}^T \Omega(t, f),$$

where $\mathbf{a}_j(\mathbf{x}) = (a_{j,1}(\mathbf{x}), \dots, a_{j,K}(\mathbf{x}))^T$, $\mathbf{b}_i = (b_{i,1}, \dots, b_{i,K})^T$, and $\mathbf{c}_{i,j} = (c_{i,j,1}, \dots, c_{i,j,K})^T$ are the corresponding basis coefficient vectors to be estimated from the data.

Let $Y_{i,j}(\mathbf{t}, \mathbf{f}) \in \mathbb{R}^{T \times F}$ and $\mathcal{E}_{i,j}(\mathbf{t}, \mathbf{f}) \in \mathbb{R}^{T \times F}$ denote the evaluations of $Y_{i,j}(t, f)$ and $\mathcal{E}_{i,j}(t, f)$ over the grid $\mathbf{t} \times \mathbf{f}$. We define the basis evaluation matrix as $\mathcal{O} = \psi(\mathbf{f}) \otimes \phi(\mathbf{t}) \in \mathbb{R}^{(TF) \times K}$, where $\phi(\mathbf{t}) \in \mathbb{R}^{T \times K_T}$ and $\psi(\mathbf{f}) \in \mathbb{R}^{F \times K_F}$ correspond to the evaluations of $\phi(t)$ and $\psi(f)$ over \mathbf{t} and \mathbf{f} , respectively. With this representation, the discretized version of model (1) can be expressed in vectorized form as

$$(3) \quad \mathbf{y}_{i,j} = \mathcal{O}(\mathbf{a}_j(\mathbf{x}_i) + \mathbf{b}_i + \mathbf{c}_{i,j}) + \boldsymbol{\epsilon}_{i,j}, \quad i = 1, \dots, n, \quad j \in \mathcal{J}_i,$$

where $\mathbf{y}_{i,j} = \text{Vec}(Y_{i,j}(\mathbf{t}, \mathbf{f}))$ and $\boldsymbol{\epsilon}_{i,j} = \text{Vec}(\mathcal{E}_{i,j}(\mathbf{t}, \mathbf{f}))$, with $\text{Vec}(\cdot)$ denoting column-wise vectorization.

2.2. Model reparametrization. For efficient posterior inference (see Section 2.4), we reparameterize (3) using an orthogonalized basis matrix $\tilde{\mathcal{O}} = \tilde{\psi}(\mathbf{f}) \otimes \tilde{\phi}(\mathbf{t})$, where $\tilde{\psi}(\mathbf{f}) = \psi(\mathbf{f})\mathbf{V}_\psi$ and $\tilde{\phi}(\mathbf{t}) = \phi(\mathbf{t})\mathbf{V}_\phi$ are rotated versions of the original marginal basis evaluations $\psi(\mathbf{f})$ and $\phi(\mathbf{t})$. The rotated basis functions are given by $\tilde{\psi}(f) = \mathbf{V}_\psi^T \psi(f)$ and $\tilde{\phi}(t) = \mathbf{V}_\phi^T \phi(t)$, in which the rotation matrices \mathbf{V}_ϕ and \mathbf{V}_ψ are obtained via the SVD of the marginal basis evaluations: $\psi(\mathbf{f}) = \mathbf{U}_\psi \boldsymbol{\Lambda}_\psi \mathbf{V}_\psi^T$ and $\phi(\mathbf{t}) = \mathbf{U}_\phi \boldsymbol{\Lambda}_\phi \mathbf{V}_\phi^T$. We assume that $\psi(\mathbf{f})$ and $\phi(\mathbf{t})$ have full column rank. Under this assumption, $\tilde{\mathcal{O}}^T \tilde{\mathcal{O}} = \text{Diag}(d_{(1)}, \dots, d_{(K)})$, where $d_{(k)} > 0$ for $k = 1, \dots, K$. We then reparameterize (3) as

$$(4) \quad \mathbf{y}_{i,j} = \tilde{\mathcal{O}}(\boldsymbol{\alpha}_j(\mathbf{x}_i) + \boldsymbol{\gamma}_i + \boldsymbol{\omega}_{i,j}) + \boldsymbol{\epsilon}_{i,j}, \quad i = 1, \dots, n, \quad j \in \mathcal{J}_i,$$

where the reparametrized coefficients $\boldsymbol{\alpha}_j(\mathbf{x}_i) = (\mathbf{V}_\psi \otimes \mathbf{V}_\phi)^T \mathbf{a}_j(\mathbf{x}_i)$, $\boldsymbol{\gamma}_i = (\mathbf{V}_\psi \otimes \mathbf{V}_\phi)^T \mathbf{b}_i$, and $\boldsymbol{\omega}_{i,j} = (\mathbf{V}_\psi \otimes \mathbf{V}_\phi)^T \mathbf{c}_{i,j}$ are rotated versions of $\mathbf{a}_j(\mathbf{x}_i)$, \mathbf{b}_i , and $\mathbf{c}_{i,j}$ in (3). This reparameterization, following Sun and Kowal (2025), allows the random effect functions $\mathcal{B}_i(t, f)$ and $\mathcal{C}_{i,j}(t, f)$ in (2) to be flexibly modeled. A posterior sampling framework is introduced in Section 2.4 for $\boldsymbol{\alpha}_j(\mathbf{x})$, $\boldsymbol{\gamma}_i$ and $\boldsymbol{\omega}_{i,j}$ in (4), which can be transformed back to the original coefficients $\mathbf{a}_j(\mathbf{x})$, \mathbf{b}_i , and $\mathbf{c}_{i,j}$ in (2).

2.3. Covariate-dependent decomposition of fixed effects. To yield a parsimonious and interpretable representation of $\mathcal{A}_j(\mathbf{x})$ in model (1), we represent the fixed effects coefficients $\boldsymbol{\alpha}_j(\mathbf{x})$ in (4) using a novel covariate-dependent variant of the CANDECOMP/PARAFAC (CP) decomposition (Kolda and Bader, 2009). Specifically, we define $\boldsymbol{\alpha}_j(\mathbf{x}) = \text{Vec}(\tilde{\mathbf{A}}_j(\mathbf{x})) \in \mathbb{R}^K$, where $\tilde{\mathbf{A}}_j(\mathbf{x}) \in \mathbb{R}^{K_T \times K_F}$ admits a rank- R CP decomposition:

$$(5) \quad \tilde{\mathbf{A}}_j(\mathbf{x}) = \sum_{r=1}^R \lambda_{j,r}(\mathbf{x}) \mathbf{u}_r \mathbf{v}_r^T.$$

This decomposition expresses $\tilde{\mathbf{A}}_j(\mathbf{x})$ as a covariate-weighted sum of rank-one matrix components $\mathbf{u}_r \mathbf{v}_r^T$, $r = 1, \dots, R$, with $R \leq \min(K_T, K_F)$. The factor loading vectors $\mathbf{u}_r \in \mathbb{R}^{K_T}$ and $\mathbf{v}_r \in \mathbb{R}^{K_F}$ represent marginal basis coefficients for the time and frequency dimensions, respectively. The covariate-dependent and component-specific weights $\lambda_{j,r}(\mathbf{x})$ are modeled as linear functions of $\mathbf{x} \in \mathbb{R}^p$: $\lambda_{j,r}(\mathbf{x}) = \boldsymbol{\delta}_{j,r}^T \mathbf{x}$, where $\boldsymbol{\delta}_{j,r} \in \mathbb{R}^p$. To ensure identifiability of (5), we assume that the factor matrices $\mathbf{U} = (\mathbf{u}_1, \dots, \mathbf{u}_R) \in \mathcal{V}_R(\mathbb{R}^{K_T})$ and $\mathbf{V} = (\mathbf{v}_1, \dots, \mathbf{v}_R) \in \mathcal{V}_R(\mathbb{R}^{K_F})$ lie on Stiefel manifolds, satisfying $\mathbf{U}^T \mathbf{U} = \mathbf{I}_R$ and $\mathbf{V}^T \mathbf{V} = \mathbf{I}_R$, where \mathbf{I}_R denotes the $R \times R$ identity matrix. When the rank R is small, (5) provides a low-rank representation of $\tilde{\mathbf{A}}_j(\mathbf{x})$, effectively regularizing the fixed-effect basis coefficients to prevent overfitting (see Section 2.4.4 for an automatic rank selection as part of posterior inference).

Building on (5), $\mathcal{A}_j(\mathbf{x})$ in the two-way functional domain (2) can be expressed as

$$(6) \quad \mathcal{A}_j(\mathbf{x})(t, f) = \sum_{r=1}^R \lambda_{j,r}(\mathbf{x}) \phi_r^*(t) \psi_r^*(f),$$

where $\phi_r^*(t) = \mathbf{u}_r^T \tilde{\phi}(t)$ and $\psi_r^*(f) = \mathbf{v}_r^T \tilde{\psi}(f)$. $\phi_r^*(t)$ and $\psi_r^*(f)$ can be interpreted as marginal “principal” functions along the time and frequency domains, respectively, which often carry neurologically meaningful interpretations in EEG studies (see Section 4 for illustration). The products $\phi_r^*(t) \psi_r^*(f)$ define two-way “base” patterns that are shared across conditions and act as building blocks for $\mathcal{A}_j(\mathbf{x})(t, f)$. Each “base” pattern is scaled by a condition- and covariate-dependent weight $\lambda_{j,r}(\mathbf{x})$, allowing subject characteristics to modulate the expression of this “base” pattern. When $\mathbf{x}_i = 1$ for all i , the fixed effect (6) reduces to the condition-specific population mean surface.

2.4. Efficient posterior inference. We develop a fully Bayesian inference procedure for model (4), enabling estimation of the fixed effect $\mathcal{A}_j(\mathbf{x})$ and random effects \mathcal{B}_i and $\mathcal{C}_{i,j}$. Leveraging the CP decomposition in (6), our approach allows inference of $\phi_r^*(t)$ and $\psi_r^*(f)$, as well as the weights $\lambda_{j,r}(\mathbf{x})$. For computational efficiency, we build on the inference approach proposed by Sun and Kowal (2025), adapting their strategy for sampling the random effects while introducing a new sampling procedure tailored to the structured fixed effects.

Throughout this paper, the subscript (l) denotes quantities (scalars, vectors, or matrices) associated with the l -th tensor product basis function. Accordingly, $\gamma_{i,(l)}$, $\omega_{i,j,(l)}$, and $\epsilon_{i,j,(l)}$ represent the l -th elements of γ_i , $\omega_{i,j}$, and $\epsilon_{i,j}$, respectively. We assign the following priors to the random components:

$$(7) \quad \gamma_{i,(l)} | \sigma_\gamma^2 \sim N(0, \sigma_\gamma^2), \quad \omega_{i,j,(l)} | \sigma_{\omega_i}^2 \sim N(0, \sigma_{\omega_i}^2), \quad \epsilon_{i,j,(l)} | \sigma_\epsilon^2 \sim N(0, \sigma_\epsilon^2),$$

with the following hyperpriors on the variance parameters:

$$(8) \quad \sigma_\gamma^2 \sim \text{IG}(a_\gamma, b_\gamma), \quad \sigma_{\omega_i}^2 \sim \text{IG}(a_\omega, b_\omega), \quad p(\sigma_\epsilon^2) \propto 1/\sigma_\epsilon^2,$$

with $\text{IG}(a, b)$ denoting an inverse Gamma distribution with shape parameter a and scale parameter b . For $\sigma_{\omega_i}^2$, we also consider a simplified setting with homogeneous variances across subjects, i.e., $\sigma_{\omega_i}^2 = \sigma_\omega^2$ for all i . The corresponding changes to the posterior sampling procedure are supported in our implementation and detailed in Supplementary Material A. Priors for the fixed effects are introduced in Sections 2.4.3 and 2.4.4. Identifiability of model (4), under the CP representation in (5) and the priors in (7), is established in Supplementary Material B.

Notation. We denote the observed data as $\mathcal{D} = \{\mathbf{X}_{1:n}, \mathbf{Y}_{1:n}\}$, where $\mathbf{Y}_{1:n} = \{\{\mathbf{y}_{i,j}\}_{j \in \mathcal{J}_i}\}_{i=1}^n$ and $\mathbf{X}_{1:n} = \{\mathbf{x}_1, \dots, \mathbf{x}_n\}$. The variance components are collectively denoted by $\mathcal{S} = \{\sigma_\gamma^2, \sigma_\epsilon^2, \sigma_\omega^2\}$, where $\sigma_\omega^2 = \{\sigma_{\omega_1}^2, \dots, \sigma_{\omega_n}^2\}$. We denote the sets of fixed and random effect coefficients as follows: $\alpha_{1:J} = \{\alpha_1, \dots, \alpha_J\}$, $\gamma_{1:n} = \{\gamma_1, \dots, \gamma_n\}$, and $\omega_{1:n} = \{\omega_1, \dots, \omega_n\}$, where $\omega_i = \{\omega_{i,j}, j \in \mathcal{J}_i\}$. Similarly, we denote the sets of random noise as $\epsilon_{1:n} = \{\epsilon_1, \dots, \epsilon_n\}$, where $\epsilon_i = \{\epsilon_{i,j}, j \in \mathcal{J}_i\}$. We also introduce notation for the random coefficients associated with the l -th tensor product basis function: $\gamma_{(l)} = (\gamma_{1,(l)}, \dots, \gamma_{n,(l)})$ and $\omega_{(l)} = (\omega_{1,(l)}^T, \dots, \omega_{n,(l)}^T)^T$, where $\omega_{i,(l)} = (\omega_{i,j,(l)})_{j \in \mathcal{J}_i}$. The set of covariate coefficients is denoted by $\delta_{1:J,1:R} = \{\{\delta_{j,r}\}_{j=1}^J\}_{r=1}^R$. We use $\mathbf{0}_m$ and $\mathbf{1}_m$ to denote the m -dimensional column vectors of zeros and ones, respectively, and \mathbf{I}_m to denote the $m \times m$ identity matrix.

The posterior sampling procedure is summarized in Algorithm 1. Inference is conducted via a two-block Gibbs sampler (in which the subscript t denotes the sample at the t -th iteration): **Block 1:** sample the fixed and random effect coefficients $(\alpha_{1:J}, \gamma_{1:n}, \omega_{1:n} | \mathcal{S}_t, \mathcal{D})$; and **Block 2:** sample the variance components $(\mathcal{S} | \alpha_{1:J,t}, \gamma_{1:n,t}, \omega_{1:n,t}, \mathcal{D})$.

2.4.1. *Posterior sampling of the variance components.* We begin by describing **Block 2**, which involves standard conjugate updates. Sampling steps for **Block 1** are detailed in Sections 2.4.2, 2.4.3 and 2.4.4.

Let $J_i = |\mathcal{J}_i|$ denote the number of observed conditions for subject i , where $|\cdot|$ denotes set cardinality, and define $J' = \sum_{i=1}^n J_i$. In **Block 2**, we sample the variance components \mathcal{S} from their conditional posterior:

$$p(\mathcal{S}|\alpha_{1:J}, \gamma_{1:n}, \omega_{1:n}, \mathcal{D}) \propto p(\mathcal{S})p(\alpha_{1:J}, \gamma_{1:n}, \omega_{1:n}|\mathcal{S})p(\mathbf{Y}_{1:n}|\alpha_{1:J}, \gamma_{1:n}, \omega_{1:n}, \mathcal{S}, \mathbf{X}_{1:n}).$$

This yields the conjugate updates below, with derivations provided in Supplementary Material C:

$$(9) \quad \sigma_\gamma^2|\alpha_{1:J}, \gamma_{1:n}, \omega_{1:n}, \mathcal{D} \sim \text{IG}\left(a_\gamma + \frac{1}{2}nK, b_\gamma + \frac{1}{2}\sum_{i=1}^n \sum_{l=1}^K \gamma_{i,(l)}^2\right),$$

$$(10) \quad \sigma_{\omega_i}^2|\alpha_{1:J}, \gamma_{1:n}, \omega_{1:n}, \mathcal{D} \sim \text{IG}\left(a_\omega + \frac{1}{2}J_iK, b_\omega + \frac{1}{2}\sum_{j \in \mathcal{J}_i} \sum_{l=1}^K \omega_{i,j,(l)}^2\right),$$

$$(11) \quad \sigma_\epsilon^2|\alpha_{1:J}, \gamma_{1:n}, \omega_{1:n}, \mathcal{D} \sim \text{IG}\left(\frac{1}{2}TFJ', \frac{1}{2}\sum_{i=1}^n \sum_{j \in \mathcal{J}_i} \|\mathbf{y}_{i,j} - \tilde{\mathcal{O}}\beta_{i,j}(\mathbf{x}_i)\|_2^2\right),$$

where $\beta_{i,j}(\mathbf{x}_i) = \alpha_j(\mathbf{x}_i) + \gamma_i + \omega_{i,j}$.

Algorithm 1: Efficient posterior sampling algorithm

```

1 Data:  $\mathcal{D} = \{\mathbf{X}_{1:n}, \mathbf{Y}_{1:n}\}$ 
2 For  $t = 1, \dots, T$  do
3   Block 1: Sample the fixed and random effects coefficients  $(\alpha_{1:J}, \gamma_{1:n}, \omega_{1:n}|\mathcal{S}_t, \mathcal{D})$ 
4   (a) Sample  $(\alpha_{1:J}|\mathcal{S}_{t-1}, \mathcal{D})$  ▷ See Sections 2.4.3 and 2.4.4
5   (b) For  $l = 1, \dots, K$  do
6     Sample  $(\gamma_{(l)}|\alpha_{1:J,t}, \mathcal{S}_{t-1}, \mathcal{D})$  ▷ See Section 2.4.2
7   EndFor
8   (c) For  $l = 1, \dots, K$  do
9     Sample  $(\omega_{(l)}|\alpha_{1:J,t}, \gamma_{1:n,t}, \mathcal{S}_{t-1}, \mathcal{D})$  ▷ See Section 2.4.2
10  EndFor
11  Block 2: Sample the variance components  $(\mathcal{S}|\alpha_{1:J,t}, \gamma_{1:n,t}, \omega_{1:n,t}, \mathcal{D})$ 
12  (a) Sample  $(\sigma_\gamma^2|\alpha_{1:J,t}, \gamma_{1:n,t}, \omega_{1:n,t}, \mathcal{D})$  from (9)
13  (b) Sample  $(\sigma_{\omega_i}^2|\alpha_{1:J,t}, \gamma_{1:n,t}, \omega_{1:n,t}, \mathcal{D})$  from (10), for  $i = 1, \dots, n$ 
14  (c) Sample  $(\sigma_\epsilon^2|\alpha_{1:J,t}, \gamma_{1:n,t}, \omega_{1:n,t}, \mathcal{D})$  from (11)
15 EndFor
16 Return:  $\{\alpha_{1:J,t}\}_{t=1}^T, \{\gamma_{1:n,t}\}_{t=1}^T, \{\omega_{1:n,t}\}_{t=1}^T, \{\mathcal{S}_t\}_{t=1}^T$ 

```

2.4.2. *Posterior sampling of random effects.* We adopt the projection approach of Sun and Kowal (2025) to simplify (4) for efficient posterior sampling. For each $\mathbf{y}_{i,j} \in \mathbb{R}^{TF}$, we define the projection $\tilde{\mathbf{y}}_{i,j} = (\tilde{\mathcal{O}}^T \tilde{\mathcal{O}})^{-1} \tilde{\mathcal{O}}^T \mathbf{y}_{i,j} \in \mathbb{R}^K$, which yields the reduced model:

$$(12) \quad \tilde{\mathbf{y}}_{i,j} = \alpha_j(\mathbf{x}_i) + \gamma_i + \omega_{i,j} + \tilde{\epsilon}_{i,j},$$

where $\tilde{\epsilon}_{i,j} \sim N(\mathbf{0}_K, \sigma_\epsilon^2 \mathbf{D}^{-1})$, with $\mathbf{D} = \tilde{\mathcal{O}}^T \tilde{\mathcal{O}}$. The likelihood of (12) is proportional to that of (4), since $\exp(-\|\mathbf{y}_{i,j} - \tilde{\mathcal{O}}\beta_{i,j}(\mathbf{x}_i)\|_2^2/(2\sigma_\epsilon^2)) \propto \exp(-\|\sqrt{\mathbf{D}}(\tilde{\mathbf{y}}_{i,j} - \beta_{i,j}(\mathbf{x}_i))\|_2^2/(2\sigma_\epsilon^2))$ (a complete derivation is provided in Supplementary Material C).

We reformulate (12) by stacking parameters (across conditions and then subjects) associated with each ($l = 1, \dots, K$) tensor product basis function, yielding the following model:

$$(13) \quad \tilde{\mathbf{y}}_{(l)} = \boldsymbol{\alpha}_{(l)} + \mathbf{Z}\boldsymbol{\gamma}_{(l)} + \boldsymbol{\omega}_{(l)} + \tilde{\boldsymbol{\epsilon}}_{(l)}, \quad \boldsymbol{\epsilon}_{(l)} \sim N(\mathbf{0}_{J'}, \boldsymbol{\Sigma}_{\tilde{\epsilon}_{(l)}}),$$

where $\tilde{\mathbf{y}}_{(l)} = (\tilde{\mathbf{y}}_{1,(l)}^T, \dots, \tilde{\mathbf{y}}_{n,(l)}^T)^T$, $\tilde{\mathbf{y}}_{i,(l)} = (\tilde{y}_{i,j,(l)})_{j \in \mathcal{J}_i}$ (which represents vertical stacking across conditions $j \in \mathcal{J}_i$); $\boldsymbol{\alpha}_{(l)} = (\boldsymbol{\alpha}_{1,(l)}^T, \dots, \boldsymbol{\alpha}_{n,(l)}^T)^T$, $\boldsymbol{\alpha}_{i,(l)} = (\alpha_{j,(l)}(\mathbf{x}_i))_{j \in \mathcal{J}_i}$; $\mathbf{Z} = \text{BlockDiag}(\mathbf{1}_{J_1}, \dots, \mathbf{1}_{J_n}) \in \mathbb{R}^{J' \times n}$; $\tilde{\boldsymbol{\epsilon}}_{(l)} = (\tilde{\boldsymbol{\epsilon}}_{1,(l)}^T, \dots, \tilde{\boldsymbol{\epsilon}}_{n,(l)}^T)^T$, $\tilde{\boldsymbol{\epsilon}}_{i,(l)} = (\tilde{\epsilon}_{i,j,(l)})_{j \in \mathcal{J}_i}$; $\boldsymbol{\Sigma}_{\tilde{\epsilon}_{(l)}} = \sigma_{\tilde{\epsilon}_{(l)}}^2 \mathbf{I}_{J'}$, where $\sigma_{\tilde{\epsilon}_{(l)}}^2 = \sigma_\epsilon^2/d_{(l)}$; and $\boldsymbol{\gamma}_{(l)}$ and $\boldsymbol{\omega}_{(l)}$ are defined in Section 2.4. We assume, without loss of generality, that the indices $j \in \mathcal{J}_i$ are sorted in ascending order.

Based on model (13) and priors specified in (7), the posterior distributions of $\boldsymbol{\omega}$ and $\boldsymbol{\gamma}$ factorize over the basis indices $l = 1, \dots, K$, allowing independent sampling for each l :

$$(14) \quad p(\boldsymbol{\omega} | \boldsymbol{\alpha}, \boldsymbol{\gamma}, \mathcal{S}, \mathcal{D}) = \prod_{l=1}^K p(\boldsymbol{\omega}_{(l)} | \sigma_\omega^2) p(\tilde{\mathbf{y}}_{(l)} | \boldsymbol{\alpha}_{(l)}, \boldsymbol{\gamma}_{(l)}, \boldsymbol{\omega}_{(l)}, \sigma_{\tilde{\epsilon}_{(l)}}^2),$$

$$(15) \quad p(\boldsymbol{\gamma} | \boldsymbol{\alpha}, \mathcal{S}, \mathcal{D}) = \prod_{l=1}^K p(\boldsymbol{\gamma}_{(l)} | \sigma_\gamma^2) p(\tilde{\mathbf{y}}_{(l)} | \boldsymbol{\alpha}_{(l)}, \boldsymbol{\gamma}_{(l)}, \sigma_\omega^2, \sigma_{\tilde{\epsilon}_{(l)}}^2).$$

The likelihood terms in (14) and (15) follow directly from (13) and its marginalization over $\boldsymbol{\omega}_{(l)}$. For $l = 1, \dots, K$, the resulting posteriors are

$$(16) \quad \boldsymbol{\omega}_{(l)} | \boldsymbol{\alpha}_{(l)}, \boldsymbol{\gamma}_{(l)}, \mathcal{S}, \mathcal{D} \sim N(\mathbf{C}_{\boldsymbol{\omega}_{(l)}} \mathbf{g}_{\boldsymbol{\omega}_{(l)}}, \mathbf{C}_{\boldsymbol{\omega}_{(l)}}),$$

$$(17) \quad \boldsymbol{\gamma}_{(l)} | \boldsymbol{\alpha}_{(l)}, \mathcal{S}, \mathcal{D} \sim N(\mathbf{C}_{\boldsymbol{\gamma}_{(l)}} \mathbf{g}_{\boldsymbol{\gamma}_{(l)}}, \mathbf{C}_{\boldsymbol{\gamma}_{(l)}}),$$

where $\mathbf{C}_{\boldsymbol{\omega}_{(l)}} = (\boldsymbol{\Sigma}_\omega^{-1} + \boldsymbol{\Sigma}_{\epsilon_{(l)}}^{-1})^{-1} \in \mathbb{R}^{J' \times J'}$, $\mathbf{g}_{\boldsymbol{\omega}_{(l)}} = \boldsymbol{\Sigma}_{\epsilon_{(l)}}^{-1} (\tilde{\mathbf{y}}_{(l)} - \boldsymbol{\alpha}_{(l)} - \mathbf{Z}\boldsymbol{\gamma}_{(l)}) \in \mathbb{R}^{J'}$, $\mathbf{C}_{\boldsymbol{\gamma}_{(l)}} = (\boldsymbol{\Sigma}_\gamma^{-1} + \mathbf{Z}^T(\boldsymbol{\Sigma}_\omega + \boldsymbol{\Sigma}_{\epsilon_{(l)}})^{-1}\mathbf{Z})^{-1} \in \mathbb{R}^{n \times n}$, $\mathbf{g}_{\boldsymbol{\gamma}_{(l)}} = \mathbf{Z}^T(\boldsymbol{\Sigma}_\omega + \boldsymbol{\Sigma}_{\epsilon_{(l)}})^{-1}(\tilde{\mathbf{y}}_{(l)} - \boldsymbol{\alpha}_{(l)}) \in \mathbb{R}^n$, $\boldsymbol{\Sigma}_\omega = \text{BlockDiag}(\sigma_{\omega_1}^2 \mathbf{I}_{J_1}, \dots, \sigma_{\omega_n}^2 \mathbf{I}_{J_n}) \in \mathbb{R}^{J' \times J'}$, and $\boldsymbol{\Sigma}_\gamma = \sigma_\gamma^2 \mathbf{I}_n$ (derivations are provided in Supplementary Material D). In (16) and (17), the covariance matrices $\mathbf{C}_{\boldsymbol{\omega}_{(l)}}$ and $\mathbf{C}_{\boldsymbol{\gamma}_{(l)}}$ are diagonal, which enables fully parallel and elementwise posterior sampling of $\boldsymbol{\omega}_{(l)}$ and $\boldsymbol{\gamma}_{(l)}$. In particular, the diagonality of $\mathbf{C}_{\boldsymbol{\gamma}_{(l)}}$ follows from

$$\mathbf{Z}^T(\boldsymbol{\Sigma}_\omega + \boldsymbol{\Sigma}_{\epsilon_{(l)}})^{-1}\mathbf{Z} = \text{Diag}\left(J_1(\sigma_{\omega_1}^2 + \sigma_\epsilon^2/d_{(l)})^{-1}, \dots, J_n(\sigma_{\omega_n}^2 + \sigma_\epsilon^2/d_{(l)})^{-1}\right).$$

2.4.3. Posterior sampling of fixed effect factor matrices. We use a Gibbs sampling procedure for posterior inference of the factor matrices \mathbf{U} and \mathbf{V} in the CP representation (5). This procedure effectively addresses two key challenges: enforcing the orthonormality constraints on \mathbf{U} and \mathbf{V} , and selecting an appropriate rank R as described in Section 2.4.4.

Let $\mathbf{u}_{-r} = \{\mathbf{u}_{r'}\}_{r' \neq r}$ and $\mathbf{v}_{-r} = \{\mathbf{v}_{r'}\}_{r' \neq r}$. We introduce the posterior sampling of $(\mathbf{u}_r | \mathbf{u}_{-r}, \mathbf{V}, \boldsymbol{\delta}_{1:J,1:R}, \mathcal{S}, \mathcal{D})$ below, with an analogous derivation for $(\mathbf{v}_r | \mathbf{v}_{-r}, \mathbf{U}, \boldsymbol{\delta}_{1:J,1:R}, \mathcal{S}, \mathcal{D})$ provided in Supplementary Material D.

We consider a Gibbs sampler that updates the columns of \mathbf{U} and \mathbf{V} in the order $\mathbf{u}_1 \rightarrow \mathbf{v}_1 \rightarrow \mathbf{u}_2 \rightarrow \mathbf{v}_2 \dots \rightarrow \mathbf{u}_R \rightarrow \mathbf{v}_R$. Due to the orthonormality constraints, each \mathbf{u}_r must lie in the orthogonal complement of the space spanned by \mathbf{u}_{-r} , denoted by $\text{Span}(\mathbf{u}_{-r})^\perp$. We construct an orthonormal basis for this orthogonal complement space, denoted by $\mathbf{B}_r \in \mathbb{R}^{K_T \times \tilde{K}_T}$, where $\tilde{K}_T = K_T - R + 1$ represents the basis dimension excluding the $R - 1$ directions

spanned by \mathbf{u}_{-r} , and represent $\mathbf{u}_r = \mathbf{B}_r \boldsymbol{\theta}_r$, where $\boldsymbol{\theta}_r \in \mathbb{S}^{\tilde{K}_T-1}$ lies on the unit sphere $\mathbb{S}^{\tilde{K}_T-1} = \{\boldsymbol{\theta} \in \mathbb{R}^{\tilde{K}_T}, \|\boldsymbol{\theta}\|_2 = 1\}$, ensuring $\|\mathbf{u}_r\|_2 = 1$ under the Euclidean norm $\|\cdot\|_2$. The orthonormal basis \mathbf{B}_r can be constructed via the QR decomposition of \mathbf{u}_{-r} , through the Gram-Schmidt process (Stewart, 1973). Posterior sampling is conducted on $\boldsymbol{\theta}_r$.

We define the “partial residuals” for subject i under condition j as $\mathbf{q}_{-r,i,j} = \tilde{\mathbf{y}}_{i,j} - \sum_{r' \neq r} (\boldsymbol{\delta}_{j,r'}^T \mathbf{x}_i) (\mathbf{v}_{r'} \otimes \mathbf{u}_{r'}) \in \mathbb{R}^K$. Stacking these vectors across J_i conditions, we obtain $\mathbf{q}_{-r,i} = (\mathbf{q}_{-r,i,j})_{j \in J_i} \in \mathbb{R}^{J_i K}$. We also define $\tilde{\mathbf{v}}_{r,i} = \tilde{\lambda}_r(\mathbf{x}_i) \otimes \mathbf{v}_r \in \mathbb{R}^{J_i K_F}$, where $\tilde{\lambda}_r(\mathbf{x}_i) = (\boldsymbol{\delta}_{j,r}^T \mathbf{x}_i)_{j \in J_i}$ denotes the weights for subject i . The stacked random components, including random effects and noise are given by $\mathbf{q}_{-r,i} - \tilde{\mathbf{v}}_{r,i} \otimes (\mathbf{B}_r \boldsymbol{\theta}_r)$, with associated covariance

$$(18) \quad \boldsymbol{\Sigma}_i = \sigma_\gamma^2 \mathbf{1}_{J_i K} \mathbf{1}_{J_i K}^T + \sigma_{\omega_i}^2 \mathbf{I}_{J_i K} + \sigma_\epsilon^2 \mathbf{I}_{J_i} \otimes \mathbf{D}^{-1} \in \mathbb{R}^{(J_i K) \times (J_i K)}.$$

Let $\tilde{\mathbf{v}}_{r,1:n} = \{\tilde{\mathbf{v}}_{r,i}\}_{i=1}^n$ and $\mathbf{q}_{-r,1:n} = \{\mathbf{q}_{-r,i}\}_{i=1}^n$. Given a prior $p(\boldsymbol{\theta}_r)$ over $\boldsymbol{\theta}_r \in \mathbb{S}^{\tilde{K}_T-1}$, the posterior distribution of $\boldsymbol{\theta}_r$ is given by

$$(19) \quad p(\boldsymbol{\theta}_r | \mathbf{v}_r, \tilde{\mathbf{v}}_{r,1:n}, \mathbf{q}_{-r,1:n}, \mathcal{S}) \propto p(\boldsymbol{\theta}_r) \exp \left(-\frac{1}{2} \left(\sum_{i=1}^n (\mathbf{q}_{-r,i} - \tilde{\mathbf{v}}_{r,i} \otimes (\mathbf{B}_r \boldsymbol{\theta}_r))^T \boldsymbol{\Sigma}_i^{-1} (\mathbf{q}_{-r,i} - \tilde{\mathbf{v}}_{r,i} \otimes (\mathbf{B}_r \boldsymbol{\theta}_r)) \right) \right) \\ \propto p(\boldsymbol{\theta}_r) \exp \left(-\frac{1}{2} \boldsymbol{\theta}_r^T \left(\sum_{i=1}^n \mathbf{B}_r^T \mathbf{H}_{r,i} \mathbf{B}_r \right) \boldsymbol{\theta}_r + \boldsymbol{\theta}_r^T \left(\mathbf{B}_r^T \sum_{i=1}^n \mathbf{w}_{r,i} \right) \right),$$

where $\mathbf{H}_{r,i} = \sum_{l_1, l_2} \tilde{v}_{r,i,l_1} \tilde{v}_{r,i,l_2} \boldsymbol{\Sigma}_{i,[l_1, l_2]}^{-1} \in \mathbb{R}^{K_T \times K_T}$ and $\mathbf{w}_{r,i} = \sum_{l_1, l_2} \tilde{v}_{r,i,l_1} \boldsymbol{\Sigma}_{i,[l_1, l_2]}^{-1} \mathbf{q}_{-r,i,[l_2]} \in \mathbb{R}^{K_T}$, with the summations taken over $l_1, l_2 = 1, \dots, J_i K_F$. Here, $\tilde{v}_{r,i,l}$ denotes the l -th element of $\tilde{\mathbf{v}}_{r,i}$; $\boldsymbol{\Sigma}_i^{-1}$ is treated as a block matrix with $(J_i K_F) \times (J_i K_F)$ blocks, each of size $K_T \times K_T$, with $\boldsymbol{\Sigma}_{i,[l_1, l_2]}^{-1} \in \mathbb{R}^{K_T \times K_T}$ denoting the (l_1, l_2) -th block; $\mathbf{q}_{-r,i}$ is treated as a block vector of $J_i K_F$ blocks, each of size K_T , with $\mathbf{q}_{-r,i,[l_2]} \in \mathbb{R}^{K_T}$ denoting the l_2 -th block. The derivation of (19) is provided in Supplementary Material D.

We consider two prior specifications for $\mathbf{U} \in \mathcal{V}_R(\mathbb{R}^{K_T})$, an uninformative (uniform) prior and a matrix von Mises–Fisher prior. Under the uniform prior $p_{\mathbf{U}}(\mathbf{U}) \propto 1$, the conditional prior on $\mathbf{u}_r | \mathbf{u}_{-r}$ is uniform in the subspace $\mathbf{u}_r \in \text{Span}(\mathbf{u}_{-r})^\perp$, corresponding to $p(\boldsymbol{\theta}_r) \propto 1$ for $\boldsymbol{\theta}_r \in \mathbb{S}^{\tilde{K}_T-1}$ (Hoff, 2007). From (19), the resulting posterior is

$$(20) \quad \boldsymbol{\theta}_r | \mathbf{v}_r, \tilde{\mathbf{v}}_{r,1:n}, \mathbf{q}_{-r,1:n}, \mathcal{S} \sim \text{Fisher-Bingham}(\mathbf{g}_{\mathbf{u}_r}, \mathbf{Q}_{\mathbf{u}_r}),$$

where $\mathbf{g}_{\mathbf{u}_r} = \mathbf{B}_r^T \sum_{i=1}^n \mathbf{w}_{r,i}$ and $\mathbf{Q}_{\mathbf{u}_r} = \mathbf{B}_r^T (\sum_{i=1}^n \mathbf{H}_{r,i}) \mathbf{B}_r$. The Fisher–Bingham distribution with parameters $(\boldsymbol{\mu}_0, \mathbf{S}_0)$ has density $f_{\text{FB}}(\boldsymbol{\theta}) \propto \exp(\boldsymbol{\mu}_0^T \boldsymbol{\theta} - \boldsymbol{\theta}^T \mathbf{S}_0 \boldsymbol{\theta} / 2)$ (Hoff, 2009), and samples can be efficiently drawn using the method of Kent, Ganeiber and Mardia (2018). Alternatively, prior information about the “principal” functions can be incorporated through a matrix von Mises–Fisher (MvMF) prior on \mathbf{U} with directional preference parameter $\mathbf{F} \in \mathcal{V}_R(\mathbb{R}^{K_T})$ and concentration parameter $\nu > 0$. The MvMF prior takes the form $f_{\text{MvMF}}(\mathbf{U}) \propto \exp(\nu \text{trace}(\mathbf{F}^T \mathbf{U})) = \exp\left(\nu \sum_{r=1}^R \mathbf{u}_r^T \mathbf{f}_r\right)$, where \mathbf{f}_r denotes the r -th column of \mathbf{F} , leading to an exponential prior $p(\boldsymbol{\theta}_r) \propto \exp(\nu \boldsymbol{\theta}_r^T \mathbf{B}_r^T \mathbf{f}_r)$ for $\boldsymbol{\theta}_r \in \mathbb{S}^{\tilde{K}_T-1}$ (Hoff, 2009). The resulting posterior distribution of $\boldsymbol{\theta}_r$ remains Fisher–Bingham as in (20), with the same $\mathbf{Q}_{\mathbf{u}_r}$ and an updated $\mathbf{g}_{\mathbf{u}_r} = \mathbf{B}_r^T \sum_{i=1}^n \mathbf{w}_{r,i} + \nu \mathbf{B}_r^T \mathbf{f}_r$.

2.4.4. Posterior sampling of covariate coefficients. For rank selection, we introduce a sparsity-inducing prior on the coefficient vectors $\boldsymbol{\delta}_{j,r}$ to shrink coefficients corresponding to redundant ranks. Shrinkage-based rank selection has been explored using the multiplicative gamma process prior (MGPP) (Bhattacharya and Dunson, 2011; Shamsioian et al., 2022),

which assumes decreasing importance for ranks $r = 1, \dots, R$. In contrast, our shrinkage prior imposes no ordering on rank importance, providing greater flexibility in exploring the parameter space. This flexibility is particularly advantageous given the strong dependencies among $\mathbf{u}_1, \dots, \mathbf{u}_R$ and $\mathbf{v}_1, \dots, \mathbf{v}_R$ due to orthogonality constraints on \mathbf{U} and \mathbf{V} , which makes additional rank-order assumptions overly restrictive and causes slow MCMC mixing.

Motivated by the spike-and-slab LASSO (SSL) (Ročková, 2018) prior originally proposed for sparse mean estimation, we specify the following hierarchical prior

$$(21) \quad \boldsymbol{\delta}_{j,r} | \tau_r \sim N(\mathbf{0}_p, \tau_r \boldsymbol{\Sigma}_{\delta_j}),$$

where $\tau_r > 0$ controls the contribution of component r , and $\boldsymbol{\Sigma}_{\delta_j}$ is a user-specified matrix encoding prior beliefs about the structure of $\boldsymbol{\delta}_{j,r}$. When τ_r takes small values, $\boldsymbol{\delta}_{1,r}, \dots, \boldsymbol{\delta}_{J,r}$ are shrunk toward $\mathbf{0}_p$, suggesting negligible contribution from component r . To encourage low-rank structures in the CP decomposition (5), we impose an SSL-inspired prior on τ_r :

$$(22) \quad p(\tau_r | m_r) = f_{\text{HL},h_1}(\tau_r)^{m_r} f_{\text{HL},h_0}(\tau_r)^{1-m_r}, \quad p(m_r | \pi) = \text{Bernoulli}(\pi), \quad \pi \sim \text{Beta}(a_\delta, b_\delta),$$

where $f_{\text{HL},h}(\tau) = \exp(-\tau/h)/h$ is the density of the half-Laplace distribution with scale parameter h . The construction in (22) defines a mixture of two half-Laplace distributions for τ_r with scales h_0 and h_1 ($h_0 < h_1$) and mixing proportion π . The “spike” component (with scale h_0) promotes strong shrinkage of τ_r toward zero, pruning redundant ranks, while the “slab” component (with scale h_1) permits larger values of τ_r . The binary indicator m_r determines whether rank r is assigned to the “spike” ($m_r = 0$) or “slab” ($m_r = 1$) component.

At each MCMC iteration, after updating \mathbf{U} and \mathbf{V} (Section 2.4.3), we perform posterior sampling via Steps (1) to (4) below. The derivations are in Supplementary Material D. For notational convenience, we define: $\boldsymbol{\tau}_{1:R} = \{\tau_r\}_{r=1}^R$, $\boldsymbol{\tau}_{-r} = \{\tau_{r'}\}_{r' \neq r}$, $\mathbf{m}_{1:R} = \{m_r\}_{r=1}^R$, $\mathbf{m}_{-r} = \{m_{r'}\}_{r' \neq r}$, $\boldsymbol{\delta}_{-(j,r)} = \{\boldsymbol{\delta}_{j',r'}\}_{(j',r') \neq (j,r)}$, and $\boldsymbol{\Xi}_{i,r} = \mathbf{x}_i (\mathbf{v}_r \otimes \mathbf{u}_r)^T$.

- **Step (1):** For $j = 1, \dots, J$ and $r = 1, \dots, R$, sample

$$\boldsymbol{\delta}_{j,r} | \pi, \boldsymbol{\tau}_{1:R}, \mathbf{m}_{1:R}, \boldsymbol{\delta}_{-(j,r)}, \mathbf{U}, \mathbf{V}, \mathcal{S}, \mathcal{D} \sim N(\mathbf{C}_{\delta_{j,r}} \mathbf{g}_{\delta_{j,r}}, \mathbf{C}_{\delta_{j,r}}),$$

where $\mathbf{C}_{\delta_{j,r}} = (\tau_r^{-1} \boldsymbol{\Sigma}_{\delta_j}^{-1} + \sum_{i=1}^n \boldsymbol{\Delta}_{i,j,r})^{-1}$, $\mathbf{g}_{\delta_{j,r}} = \sum_{i=1}^n \boldsymbol{\chi}_{i,j,r}$, $\boldsymbol{\Delta}_{i,j,r} = \boldsymbol{\Xi}_{i,r} \boldsymbol{\Sigma}_{i,(j,j)}^{-1} \boldsymbol{\Xi}_{i,r}^T$, and $\boldsymbol{\chi}_{i,j,r} = \boldsymbol{\Xi}_{i,r} \left(\boldsymbol{\Sigma}_{i,(j,j)}^{-1} \mathbf{q}_{-r,i,j} + \sum_{j' \in \mathcal{J}_i, j' \neq j} \left(\boldsymbol{\Sigma}_{i,(j',j)}^{-1} (\mathbf{q}_{-r,i,j'} - (\boldsymbol{\delta}_{j',r}^T \mathbf{x}_i) \mathbf{v}_r \otimes \mathbf{u}_r) \right) \right)$. Here, $\boldsymbol{\Sigma}_i^{-1}$ is partitioned into $J_i \times J_i$ blocks, each of size $K \times K$, with $\boldsymbol{\Sigma}_{i,(j_1,j_2)}^{-1}$ denoting the (j_1, j_2) -th block.

- **Step (2):** For $r = 1, \dots, R$, sample

$$\tau_r | \pi, \boldsymbol{\tau}_{-r}, \mathbf{m}_{1:R}, \boldsymbol{\delta}_{1:J,1:R}, \mathbf{U}, \mathbf{V}, \mathcal{S}, \mathcal{D} \sim \text{GIG} \left(\frac{2}{h(m_r)}, \sum_{j=1}^J \boldsymbol{\delta}_{j,r}^T \boldsymbol{\Sigma}_{\delta_j}^{-1} \boldsymbol{\delta}_{j,r}, -\frac{pJ}{2} + 1 \right),$$

where $h(1) = h_1, h(0) = h_0$, and $\text{GIG}(a, b, c)$ denotes the generalized inverse Gaussian (GIG) distribution with parameters $a > 0, b > 0$, and $c \in \mathbb{R}$. For computational efficiency, we approximate sampling from $\text{GIG}(a, b, c)$ using its mode: $(c - 1 + \sqrt{(c - 1)^2 + ab})/a$.

- **Step (3):** For $r = 1, \dots, R$, sample

$$m_r | \pi, \boldsymbol{\tau}_{1:R}, \mathbf{m}_{-r}, \boldsymbol{\delta}_{1:J,1:R}, \mathbf{U}, \mathbf{V}, \mathcal{S}, \mathcal{D} \sim \text{Bernoulli}(\tilde{p}),$$

where $\tilde{p} = \pi f_{\text{HL},h_1}(\tau_r) / (\pi f_{\text{HL},h_1}(\tau_r) + (1 - \pi) f_{\text{HL},h_0}(\tau_r))$.

- **Step (4):** Sample

$$\pi | \boldsymbol{\tau}_{1:R}, \mathbf{m}_{1:R}, \boldsymbol{\delta}_{1:J,1:R}, \mathbf{U}, \mathbf{V}, \mathcal{S}, \mathcal{D} \sim \text{Beta}(\tilde{a}, \tilde{b}),$$

where $\tilde{a} = a_\delta + \sum_{r=1}^R m_r$ and $\tilde{b} = b_\delta + R - \sum_{r=1}^R m_r$.

To perform rank selection with shrinkage priors, a common approach is to specify a moderately large R (exceeding the true rank) and select the rank by thresholding component-specific parameters (τ_r in our case), followed by restricting inference to the selected components or refitting the model with the selected rank. Instead, we implement a “warm-start” strategy that dynamically adds or removes ranks during sampling, which improves sampling efficiency and avoids repeated model refitting. This approach is detailed in Section 3.1.

3. Simulation. We refer to the proposed method in Section 2 as Bayesian Mixed-Effects Functional Model (**BMEF**), which jointly addresses three challenges (i) multilevel data structure, (ii) two-way functional data, and (iii) subject-level covariates. Since no existing method simultaneously addresses all three challenges, we benchmark our method against representative alternatives that address two of these challenges, either directly or with minor adaptations. Our comparison includes three existing methods and two variants of our proposal:

- **MHPCA**: Multilevel Hybrid Principal Components Analysis (Campos et al., 2022), which addresses (i) and can be adapted to (ii) (but does not address (iii));
- **BALMF**: Bayesian Analysis of Longitudinal and Multidimensional Functional Data (Shamshoian et al., 2022), which addresses (ii) and (iii) (but not (i));
- **FLFOSR**: Fast Longitudinal Function-on-Scalar Regression (Sun and Kowal, 2025), which addresses (i) and (iii) (but not (ii)).
- **BMEF-1**: The proposed Bayesian Mixed-Effects Functional Model with heterogeneous variances (see Section 2), which addresses (i), (ii), and (iii).
- **BMEF-2**: The proposed Bayesian Mixed-Effects Functional Model with homogeneous variance (see Section 2 and Supplementary Material A), which addresses (i), (ii), and (iii).

3.1. Set up. We generated data from model (1) under the basis expansion in (2) and the CP decomposition in (5). The simulation setup includes $J = 3$ experimental conditions, with functional responses evaluated on a $T \times F = 50 \times 50$ grid evenly spaced over the $[0, 1]^2$ domain. Let $\mathbf{x}_i = (x_{i,1}, \dots, x_{i,p})^T$ denote the covariate vector for subject i , assumed to be i.i.d. realizations of a random vector $\mathbf{X} = (X_1, \dots, X_p)^T$. We considered three scenarios with increasing complexity in the fixed effects structure, where $\mathcal{A}_j(\mathbf{x}_i)$ depends on

- S_1 : Condition only, with $X_1 = 1$.
- S_2 : Condition and one feature, with $X_1 = 1$ and $X_2 \sim \text{Unif}(-3, 3)$.
- S_3 : Condition and two features, with $X_1 = 1$, $X_2 \sim \text{Unif}(-3, 3)$, and $X_3 \sim \text{Bernoulli}(0.5)$.

For each scenario $S \in \{S_1, S_2, S_3\}$, we considered CP ranks $R \in \{2, 3, 4\}$. For each $S \times R$ combination, we evaluated model performance under two variance settings

- H_1 : Homogeneous variance, with $\sigma_{\omega_i}^2 = 0.4^2$, for $i = 1, \dots, n$
- H_2 : Heterogeneous variance, with $\sigma_{\omega_i}^2 \sim \text{Unif}(0.2^2, 1)$ independently for $i = 1, \dots, n$.

We fixed $\sigma_\gamma^2 = 0.4^2$ and $\sigma_\epsilon^2 = 0.1^2$, and generated γ_i , $\omega_{i,j}$, and $\epsilon_{i,j}$ based on (7). We used natural cubic B-splines with evenly spaced interior knots as the marginal bases $\phi(t)$ and $\psi(f)$, setting dimensions $K_T = K_F = 6$. The factor matrices \mathbf{U} and \mathbf{V} were sampled uniformly from the Stiefel manifold $\mathbf{V} \in \mathcal{V}_R(\mathbb{R}^6)$, using the method of Stewart (1980) implemented in the R package `pracma` (Borchers, 2022). For $j = 1, \dots, J$ and $r = 1, \dots, R$, each element of $\delta_{j,r}$ was independently drawn from the mixture: $0.5\text{Unif}(-1, -0.5) + 0.5\text{Unif}(0.5, 1)$.

MHPCA of Campos et al. (2022) was originally developed for multilevel data with one discrete and one functional dimension but it extends naturally to two-way functional data. Under this extension, the model takes the form

$$(23) \quad Y_{i,j}(t, f) = \mathcal{A}_j(t, f) + \mathcal{B}_i(t, f) + \mathcal{C}_{i,j}(t, f) + \mathcal{E}_{i,j}(t, f),$$

where \mathcal{A}_j is estimated by smoothing the average of the functional observations $\mathcal{Y}_{i,j}(\mathbf{t}, \mathbf{f})$ across subjects, and \mathcal{B}_i and $\mathcal{C}_{i,j}$ are modeled using eigenfunctions of the subject- and subject-by-condition-level covariances, respectively. The noise term $\mathcal{E}_{i,j}(t, f)$ is assumed to be independent of t and f . Estimation is performed under a weak separability assumption, where the eigenfunctions of the two-way covariance are constructed from those of the marginal covariances smoothed using tensor product bases. Unlike the original implementation of **MHPCA**, which uses discrete-continuous bases, we used continuous marginal bases in both dimensions to accommodate two-way functional covariances, with 6 basis functions per dimension. The implementation was adapted from the R package `mhpca` (Campos and Senturk, 2025).

For **BALMF**, we adopted the implementation from the R package `LFBayes` (Shamshoian et al., 2020). Since **BALMF** does not support multilevel data, we fit separate models for each condition $j = 1, \dots, J$, yielding the following model:

$$Y_{i,j}(\mathbf{x}_i)(t, f) = \mathcal{A}_j(\mathbf{x}_i)(t, f) + \mathcal{C}_{i,j}(t, f) + \mathcal{E}_{i,j}(t, f), \quad i \in \{i', j \in \mathcal{J}'\}.$$

BALMF shares several features with our proposed **BMEF**, including the use of tensor-product bases to approximate $\mathcal{A}_j(\mathbf{x})$ and $\mathcal{C}_{i,j}$, and a covariate-dependent factor model for $\mathcal{A}_j(\mathbf{x})$, however, its factor model relies on a Tucker-type decomposition, which is unidentifiable and less parsimonious than the CP decomposition used in **BMEF**. We applied **BALMF** with natural cubic B-splines (6 knots) as marginal bases and set the factor ranks to 4×4 , resulting in greater model complexity than our highest CP-rank setting ($R = 4$). **BALMF** incorporates a rank-regularization prior that avoids manual rank selection (Shamshoian et al., 2022). We ran the MCMC sampler for 1000 burn-in iterations followed by 400 posterior draws.

FLFOSR was originally developed for one-way functional data (Sun and Kowal, 2025). To apply it to two-way functional observations, we fit separate models for each frequency grid point $f \in \{f_1, \dots, f_F\}$, resulting in the following model:

$$Y_{i,j,f}(\mathbf{x}_i)(t) = \mathcal{A}_{j,f}(\mathbf{x}_i)(t) + \mathcal{B}_{i,j,f}(t) + \mathcal{C}_{i,j,f}(t) + \mathcal{E}_{i,j,f}(t),$$

where $\mathcal{A}_{j,f}(\mathbf{x}_i)$, $\mathcal{B}_{i,j,f}$, and $\mathcal{C}_{i,j,f}$ are one-way functions, and $\mathcal{E}_{i,j,f}(t)$ represents random noise independent of t . We used the R package `FLFOSR` (Sun, 2023) to fit the model, approximating $\mathcal{A}_{j,f}(\mathbf{x}_i)(t)$, $\mathcal{B}_{i,j,f}(t)$, and $\mathcal{C}_{i,j,f}(t)$ using cubic P-splines of dimension 6. The original implementation of **FLFOSR** assumes a common fixed effect function shared across conditions. To ensure a fair comparison with **BMEF**, we modified the input design matrix to include condition-specific indicators and their interactions with covariates, enabling the fixed effect function $\mathcal{A}_{j,f}$ to vary across both conditions and covariates. We ran the method with 1000 burn-in iterations followed by 400 sampling iterations. Posterior draws of $\mathcal{A}_{j,f}(\mathbf{x}_i)(t, f)$, $\mathcal{B}_{i,j,f}(t, f)$, and $\mathcal{C}_{i,j,f}(t, f)$ were obtained by concatenating the posterior samples of $\mathcal{A}_{j,f}(\mathbf{x}_i)$, $\mathcal{B}_{i,j,f}$, and $\mathcal{C}_{i,j,f}$ over $f \in \{f_1, \dots, f_F\}$.

For **BMEF-1** and **BMEF-2**, we specified the marginal bases $\phi(t)$ and $\psi(f)$ as natural cubic B-splines with dimensions $K_T = K_F = 6$ and evenly spaced interior knots. The prior parameters were set as follows: $a_\gamma = 3$, $b_\gamma = 0.5$, $a_\omega = 3$, and $b_\omega = 0.5$ in (8); $\Sigma_{\delta_j} = 5\mathbf{I}_p$ in (21); $a_\delta = 1$, $b_\delta = 1$, $h_1 = 1$, and $h_0 = 0.01$ in (22). We used uniform priors for \mathbf{U} and \mathbf{V} . The MCMC sampler was run with 800 burn-in iterations and 400 sampling iterations. To select the CP rank, we used a “warm-start” strategy that adaptively adjusts the rank during sampling to accelerate convergence. The algorithm begins with rank 1 and evaluates whether to add or remove ranks every 100 iterations. If all τ_r exceed a threshold (set to 0.05), an additional rank is introduced. If any τ_r falls below the threshold, the corresponding rank is removed. Once a rank is removed, the algorithm does not consider adding new ranks in subsequent iterations. When an irrelevant rank r' is introduced, our approach yields sparser estimates for $\delta_{j,r'}$ compared to forward selection without a shrinkage prior, and the values of τ_r provide

a practical and effective guide for rank selection. For the competing methods (**MHPCA**, **BALMF**, **FLFOSR**), any model parameters not mentioned above were set to their default values.

3.2. Evaluation metrics. We conducted 100 independent simulation runs, randomly generating \mathbf{x}_i , $\boldsymbol{\alpha}_j$, $\boldsymbol{\gamma}_i$, $\boldsymbol{\omega}_{i,j}$, and $\boldsymbol{\epsilon}_{i,j}$ in each run. The performance of the methods under comparison was evaluated in the following aspects.

3.2.1. Estimation of fixed effects. We evaluated the estimation accuracy of \mathcal{A}_j using mean squared error (MSE) defined as $\text{MSE}(\mathcal{A}) = \sum_{i=1}^n \sum_{j=1}^J \|\hat{\mathcal{A}}_j(\mathbf{x}_i)(\mathbf{t}, \mathbf{f}) - \mathcal{A}_j(\mathbf{x}_i)(\mathbf{t}, \mathbf{f})\|_F^2 / (nJ)$, where $\|\cdot\|_F$ denotes the Frobenius norm. For Bayesian methods (**BALMF**, **FLFOSR**, **BMEF-1**, and **BMEF-2**), $\hat{\mathcal{A}}_j(\mathbf{x}_i)(\mathbf{t}, \mathbf{f})$ denotes the posterior mean; for **MHPCA**, $\hat{\mathcal{A}}_j(\mathbf{x}_i)(\mathbf{t}, \mathbf{f})$ corresponds to the point estimate.

In S_2 and S_3 settings, we evaluated the accuracy of **BALMF**, **FLFOSR**, **BMEF-1**, and **BMEF-2** in estimating the covariate effects using a contrast mean squared error (CMSE). For X_2 in S_2 and S_3 , and X_3 in S_3 , we define $\text{CMSE}(X_k) = \sum_{i=1}^n \sum_{j=1}^J \|\widehat{\text{Diff}}(X_k)(\mathbf{t}, \mathbf{f}) - \text{Diff}(X_k)(\mathbf{t}, \mathbf{f})\|_F^2 / (nJ)$, for $k \in \{2, 3\}$, where $\text{Diff}(X_k)$ quantifies the effect of changing X_k from 0 to 1, while conditioning on the other covariates being held fixed. For S_2 , $\text{Diff}(X_2)(\mathbf{t}, \mathbf{f}) = \mathcal{A}_j((X_1, 1))(\mathbf{t}, \mathbf{f}) - \mathcal{A}_j((X_1, 0))(\mathbf{t}, \mathbf{f})$; for S_3 , $\text{Diff}(X_2)(\mathbf{t}, \mathbf{f}) = \mathcal{A}_j((X_1, 1, X_3))(\mathbf{t}, \mathbf{f}) - \mathcal{A}_j((X_1, 0, X_3))(\mathbf{t}, \mathbf{f})$, and $\text{Diff}(X_3) = \mathcal{A}_j((X_1, X_2, 1))(\mathbf{t}, \mathbf{f}) - \mathcal{A}_j((X_1, X_2, 0))(\mathbf{t}, \mathbf{f})$. The estimated effects, denoted $\widehat{\text{Diff}}(X_2)$ and $\widehat{\text{Diff}}(X_3)$, were computed by replacing \mathcal{A}_j with $\hat{\mathcal{A}}_j$. Due to the additive structure of covariate effects in the models under comparison, the values of the conditioning covariates do not affect $\text{Diff}(X_k)$ and $\widehat{\text{Diff}}(X_k)$ for $k \in \{2, 3\}$.

For **BMEF-1** and **BMEF-2**, we further evaluated their ability to correctly select the true rank R , using the sparsity-inducing prior on covariate coefficients introduced in Section 2.4.4.

3.2.2. Estimation of random effects. We used MSE to assess the accuracy of estimating subject- and subject-by-condition-level random effects. For **MHPCA**, **FLFOSR**, **BMEF-1**, and **BMEF-2**, the MSE for subject-specific effects was computed as $\text{MSE}(\mathcal{B}) = \sum_{i=1}^n \|\hat{\mathcal{B}}_i(\mathbf{t}, \mathbf{f}) - \mathcal{B}_i(\mathbf{t}, \mathbf{f})\|_F^2 / n$, and the MSE for subject-by-condition-level effects was computed for all methods as $\text{MSE}(\mathcal{C}) = \sum_{i=1}^n \sum_{j \in \mathcal{J}_i} \|\hat{\mathcal{C}}_{i,j}(\mathbf{t}, \mathbf{f}) - \mathcal{C}_{i,j}(\mathbf{t}, \mathbf{f})\|_F^2 / (nJ')$. For **FLFOSR**, **BMEF-1**, and **BMEF-2**, the estimates $\hat{\mathcal{B}}_i(\mathbf{t}, \mathbf{f})$ and $\hat{\mathcal{C}}_{i,j}(\mathbf{t}, \mathbf{f})$ correspond to the respective posterior means, while for **MHPCA**, they are point estimates. **BALMF** does not include \mathcal{B}_i in its model, and its $\hat{\mathcal{C}}_{i,j}(\mathbf{t}, \mathbf{f})$ was computed from the posterior mean.

We report results without missing conditions (i.e., $\mathcal{J}_i = \{1, \dots, J\}$ for $i = 1, \dots, n$) in Section 3.3 below. Additional simulation results for scenarios with missing conditions are reported in Supplementary Material E.

3.3. Results. We present results for the most complex setting with rank $R = 4$. Findings from other settings follow similar trends and are summarized in this section, with details provided in Supplementary Material E. Results for **MHPCA** are only reported for S_1 settings for the fixed effect, as this method does not account for covariate effects and performs substantially worse in covariate-dependent settings S_2 and S_3 . Although **MHPCA** includes \mathcal{B}_i and $\mathcal{C}_{i,j}$, their estimation is highly unstable and therefore not reported here. Figure 1 presents $\text{MSE}(\mathcal{A})$ from 100 simulation runs. Across all covariate settings (S_1 , S_2 , and S_3), **BMEF-1** and **BMEF-2** consistently achieve the lowest $\text{MSE}(\mathcal{A})$ under both variance configurations H_1 and H_2 . Notably, **BMEF-1** performs comparably to **BMEF-2** under H_1 , and outperforms **BMEF-2** under H_2 , demonstrating the flexibility of **BMEF-1** in accommodating heterogeneous variances across subjects. Figure 2 presents CMSE for estimating the covariate effects

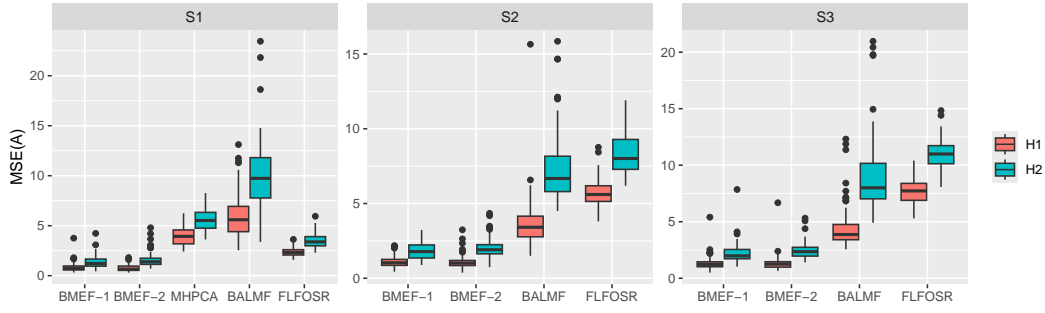


FIG 1. $MSE(\mathcal{A})$ from 100 simulation runs for rank $R = 4$, under $\{S_1, S_2, S_3\}$ and $\{H_1, H_2\}$ combinations.

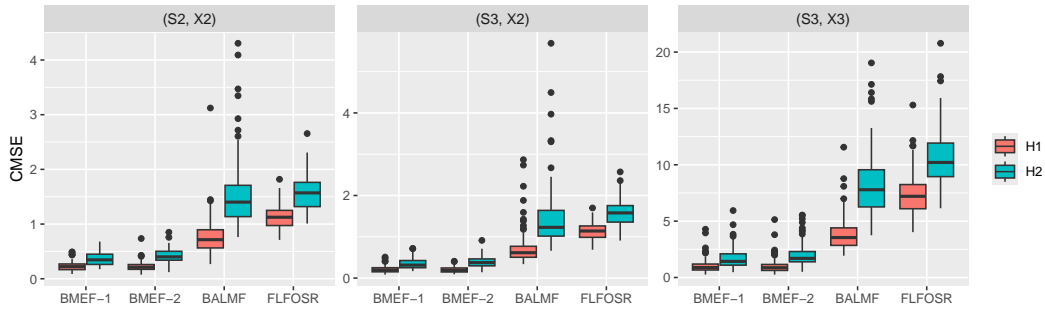


FIG 2. $CMSE$ from 100 simulation runs for rank $R = 4$, displaying $CMSE(X_2)$ for S_2 and S_3 , and $CMSE(X_3)$ for S_3 , across $\{H_1, H_2\}$ settings.

based on 100 simulations runs. Consistent with the $MSE(\mathcal{A})$ findings, **BMEF-1** and **BMEF-2** outperform all competing methods across settings. Under H_2 , **BMEF-1** achieves lower CMSEs compared to **BMEF-2**. The poor performance of **BALMF** and **FLFOSR** results from their inability to share information across dimensions and conditions. **FLFOSR** fits separate models for each frequency, ignoring the smoothness across the frequency domain. **BALMF** fits each condition independently, without incorporating subject-level random effects shared across conditions. In S_1 settings, although **MHPCA** shares the same model (23) as **BMEF-1** and **BMEF-2**, its reliance on the weak separability assumption on the functional covariances and naive use of smoothing splines to estimate the fixed effects without accounting for the random effects (Campos et al., 2022) can lead to model misspecification and inferior estimation.

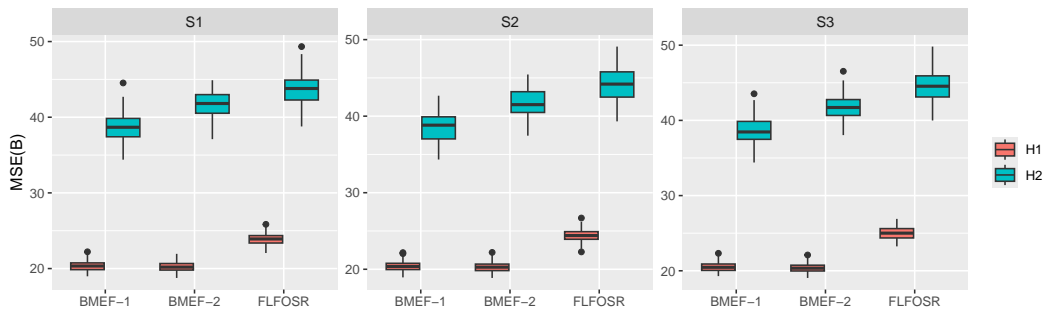


FIG 3. $MSE(\mathcal{B})$ from 100 simulation runs for rank $R = 4$, under $\{S_1, S_2, S_3\}$ and $\{H_1, H_2\}$ combinations.

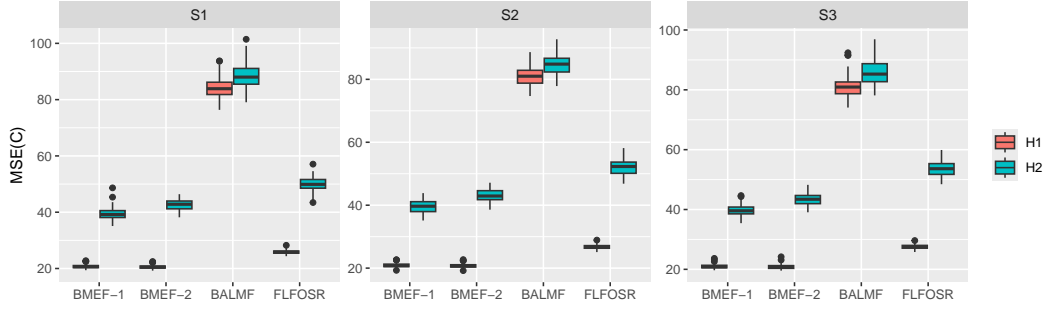


FIG 4. $MSE(C)$ from 100 simulation runs for rank $R = 4$, under $\{S_1, S_2, S_3\}$ and $\{H_1, H_2\}$ combinations.

Figure 3 and Figure 4 present the results for $MSE(B)$ and $MSE(C)$, respectively. **BALMF** is excluded from Figure 3 as it does not explicitly model B_i , instead absorbing its effect into the estimated $C_{i,j}$. Both figures show that **BMEF-1** and **BMEF-2** outperform the competing methods, with **BMEF-1** showing better performance compared to **BMEF-2** under H_2 .

Results in Supplementary Material E show that for ranks $R = 2$ and $R = 3$, all methods show similar performance patterns to those for $R = 4$, leading to the same conclusion: **BMEF-1** and **BMEF-2** consistently achieve the best performance, with **BMEF-1** showing greater flexibility under H_2 settings. As the rank increases from 2 to 4, $MSE(A)$ increases for all methods, with a more substantial increase for **BALMF** in S_1 settings and for all competitors in S_2 and S_3 settings. Across all ranks, **FLFOSR** is especially sensitive to covariate complexity, showing degraded performance from S_1 to S_3 , likely due to the increased feature dimensionality from covariate-by-condition interactions. In contrast, **BMEF-1** and **BMEF-2** maintain stable performance across settings, showing only a slight increase in $MSE(A)$ and $MSE(C)$ and comparable $MSE(B)$ with the inclusion of more covariates.

Lastly, we assessed the rank selection accuracy of **BMEF-1** and **BMEF-2** across all settings by computing the proportion of simulation runs (out of 100) in which the selected rank matched the true rank. Both methods correctly selected the true rank in 100% of the runs for S_2 and S_3 settings, and in 99% of the runs for S_1 settings, demonstrating the effectiveness of the proposed rank selection procedure. Detailed are provided in Supplementary Material E.

4. Application. Understanding the neural signatures of alcohol-related cognitive dysfunction remains an important challenge in clinical neuroscience, particularly as alcoholism is associated with altered frontal lobe activity and impaired working memory. We applied our method to an EEG dataset collected to study how alcoholism affects cognitive processing in response to visual stimuli. The dataset includes recordings from 122 subjects (77 alcoholic, 45 nonalcoholic), collected by the Neurodynamics Laboratory at the State University of New York Health Center and is available from the UCI Machine Learning Repository (Begleiter, 1995). Each subject completed 120 trials, with each trial presenting one of three visual stimulus types: a single image (C_1), a pair of matched images (C_2), or a pair of non-matched images (C_3) (Zhang et al., 1995). After excluding artifact-contaminated trials, an average of 91 usable trials per subject was retained. Time-frequency representations of EEG signals were computed using the `spectro` function from the R package `seewave` (J. Sueur, T. Aubin and C. Simonis, 2008), applying a short-time Fourier transform and yielding power spectra on a grid of $T = 21$ time points and $F = 25$ frequency points. Power was expressed in decibels (dB), and we applied $1/f$ correction (Gyurkovics et al., 2021) by subtracting the mean dB across time and subjects to reduce spectral imbalance across frequency. For each subject, the time-frequency representations were averaged across trials per condition. To focus on frontal brain activity implicated in cognitive control and working memory (Cavanagh

TABLE 1

WAIC summary (mean (SD)) for **BMEF-1** and **BMEF-2** across thresholds ($\lambda_\tau \in \{0.01, 0.05, 0.1\}$) and the three model specifications, based on 100 experimental runs. Reported values are scaled by a factor of 10^{-2} .

	BMEF-1			BMEF-2		
	$\lambda_\tau = 0.01$	$\lambda_\tau = 0.05$	$\lambda_\tau = 0.1$	$\lambda_\tau = 0.01$	$\lambda_\tau = 0.05$	$\lambda_\tau = 0.1$
BMEF-ABC	2672.4 (19.5)	2672.6 (19.3)	2672.8 (19.6)	2665.3 (19.7)	2665.2 (19.5)	2665.5 (19.7)
BMEF-AB	3842.7 (46.3)	3843.0 (46.1)	3842.9 (45.9)	3842.7 (46.3)	3843.0 (46.1)	3842.9 (45.9)
BMEF-A	5765.8 (65.4)	5765.7 (65.3)	5765.7 (65.4)	5765.8 (65.4)	5765.7 (65.3)	5765.7 (65.4)

and Frank, 2014), we analyzed data from the AFz electrode, where preliminary analyses showed representative spectral patterns across all regions.

We investigated how alcoholism (coded as a binary indicator) is associated with multi-condition EEG time-frequency responses and compared three **BMEF** model specifications of decreasing complexity. All models include an intercept and the alcoholism indicator as covariates, but differ in their random effects specification at the subject and subject-by-condition level:

- **BMEF-ABC**: Includes both subject-level (\mathcal{B}_i) and subject-by-condition-level ($\mathcal{C}_{i,j}$) random effects $Y_{i,j}(\mathbf{x})(t, f) = \mathcal{A}_j(\mathbf{x})(t, f) + \mathcal{B}_i(t, f) + \mathcal{C}_{i,j}(t, f) + \mathcal{E}_{i,j}(t, f)$
- **BMEF-AB**: Includes only subject-level random effects $Y_{i,j}(\mathbf{x})(t, f) = \mathcal{A}_j(\mathbf{x})(t, f) + \mathcal{B}_i(t, f) + \mathcal{E}_{i,j}(t, f)$
- **BMEF-A**: Includes no random effects $Y_{i,j}(\mathbf{x})(t, f) = \mathcal{A}_j(\mathbf{x})(t, f) + \mathcal{E}_{i,j}(t, f)$

For these models, we conducted inference using the **BMEF-1** and **BMEF-2** frameworks introduced in Section 3, which assume heterogeneous and homogeneous variances, respectively. For both **BMEF-1** and **BMEF-2**, for rank selection, three threshold values for τ_r in (21), denoted by $\lambda_\tau \in \{0.01, 0.05, 0.1\}$, were considered. The “warm-start” procedure introduced in Section 3.1 was adopted. Natural cubic B-splines with evenly spaced interior knots were used as marginal basis functions, with dimensions $K_T = 6$ and $K_F = 10$. These dimensions were found to be sufficient, as increasing their values did not improve the estimation of the underlying functional patterns. Other implementation details remained the same as those described in Section 3.1. The performance of each model was evaluated using Watanabe–Akaike Information Criterion (WAIC) (Vehtari, Gelman and Gabry, 2017) defined as

$$(24) \quad \text{WAIC} = -2 \left(\sum_{i=1}^n \log \left(\frac{1}{S} \sum_{s=1}^S p(\{\mathbf{y}_{i,j}\}_{j \in \mathcal{J}_i} | \Theta_s) \right) - \sum_{i=1}^n \text{Var}(\log(p(\{\mathbf{y}_{i,j}\}_{j \in \mathcal{J}_i} | \Theta_s))) \right),$$

where Θ_s denotes the set of parameters for the corresponding model specification at the s -th posterior draw, and S is the total number of posterior samples. We repeated the experiment 100 times, each time fitting all models using data from a randomly selected 80% subset of the subjects.

Table 1 summarizes WAIC values across model specifications and threshold levels $\lambda_\tau \in \{0.01, 0.05, 0.1\}$. **BMEF-ABC** consistently outperforms **BMEF-AB** and **BMEF-A**, suggesting the importance of incorporating both subject-level and subject-by-condition-level random effects \mathcal{B}_i and $\mathcal{C}_{i,j}$. The improvement from including \mathcal{B}_i (via **BMEF-AB**) over **BMEF-A** suggests substantial between-subject variability for all visual stimuli, and the additional gain from including $\mathcal{C}_{i,j}$ (via **BMEF-ABC**) suggests strong individualized responses to distinct stimulus conditions, with both sources of variability unrelated to alcoholism. Under the **BMEF-ABC** specification, **BMEF-2** yields improved performance compared to **BMEF-1**

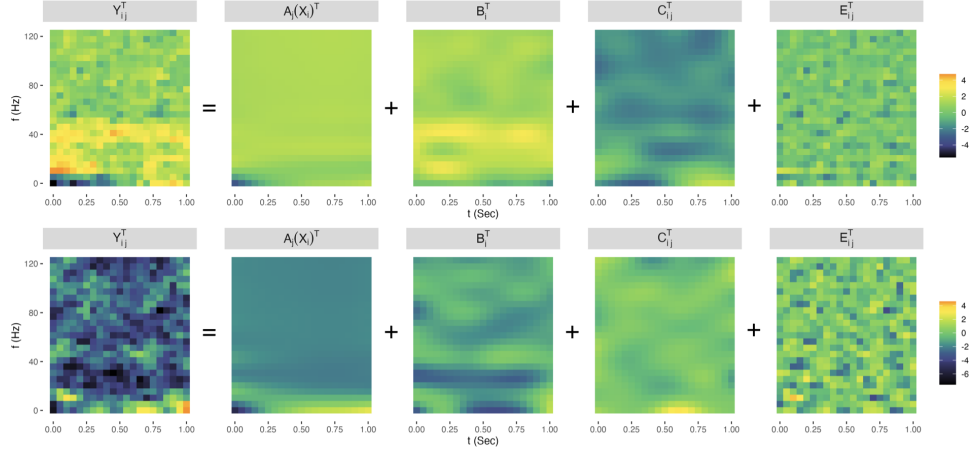


FIG 5. *Decompositions of the time-frequency response $\mathbf{Y}_{i,j} = \mathbf{A}_j(\mathbf{x}_i) + \mathbf{B}_i + \mathbf{C}_{i,j} + \mathbf{E}_{i,j}$, where $\mathbf{A}_j(\mathbf{x}_i)$, \mathbf{B}_i , $\mathbf{C}_{i,j}$, and $\mathbf{E}_{i,j}$ are evaluations of $\mathcal{A}_j(x_i)$, \mathcal{B}_i , $\mathcal{C}_{i,j}$, and $\mathcal{E}_{i,j}$ on a $\mathbf{t} \times \mathbf{f}$ grid of dimensions 21×25 . Results are shown for one representative alcoholic subject under condition C_1 (presented with “single image”) (top row) and one representative control subject under condition C_2 (presented with “matched images”) (bottom row).*

with respect to WAIC, suggesting that the heterogeneous variance assumption in **BMEF-1** may introduce unnecessary complexity and lead to overfitting. WAIC values are stable across different threshold (λ_τ) values. For **BMEF-1** and **BMEF-2**, setting $\lambda_\tau = 0.01$ typically selected rank $R = 4$, $\lambda_\tau = 0.05$ yielded variable selections of $R = 3$ or 4, and $\lambda_\tau = 0.1$ selected $R = 2$ across runs. When $R = 3$ or 4 were selected, we consistently observed two dominant “base” patterns that receive much higher weights compared to the rest. Notably, these two patterns closely matched those from the $R = 2$ model, suggesting models with $R > 2$ introduced redundant or weakly contributing components. Based on these observations, we performed the full analysis on all 122 subjects using **BMEF-2** with $\lambda_\tau = 0.1$, under the **BMEF-ABC** specification, and report the findings below.

Figure 5 illustrates the model-based decomposition of the observed time-frequency representation $\mathbf{Y}_{i,j} \in \mathbb{R}^{21 \times 25}$ for two representative subject-condition pairs: an alcoholic subject (Subject 1) under condition C_1 , and a control subject (Subject 2) under condition C_2 . The evaluations of the estimated $\mathcal{A}_j(\mathbf{x}_i)$, \mathcal{B}_i , $\mathcal{C}_{i,j}$ and $\mathcal{E}_{i,j}$ over the observed time-frequency grid are denoted by $\mathbf{A}_j(\mathbf{x}_i)$, \mathbf{B}_i , $\mathbf{C}_{i,j}$ and $\mathbf{E}_{i,j}$, respectively. From Figure 5, the fixed effect $\mathbf{A}_j(\mathbf{x}_i)$ differs notably between Subject 1 and 2, reflecting variation attributable to alcoholism and visual stimulus type. The subject-level random effect \mathbf{B}_i shows distinct time-frequency patterns between Subjects 1 and 2, particularly in the low to mid-frequency range: Subject 1 shows elevated activity around 10–40 Hz, and Subject 2 shows reduced activity around 10–30 Hz. These patterns can be observed in their corresponding raw responses $\mathbf{Y}_{i,j}$. The subject-by-condition random effect $\mathbf{C}_{i,j}$ appears smooth and captures the remaining functional structure. The residual term $\mathbf{E}_{i,j}$ appears unstructured, supporting the Gaussian noise assumption imposed by our model.

Figure 6 displays the posterior means of the fixed effect $\mathcal{A}_j(\mathbf{x}_i)$ across combinations of experimental conditions (C_1 , C_2 , and C_3) (columns) and alcoholism status (rows). Alcoholic subjects show higher estimated fixed effect values across conditions, particularly in the higher frequency bands. Additionally, the fixed effect pattern for C_2 and C_3 are more similar to each other than to C_1 , consistent with the experimental design: C_2 and C_3 involve paired visual inputs, while C_1 consists of a single image input.

Figure 7 presents the estimated rank-specific “base” patterns $\phi_r^*(t)\psi_r^*(f)$ that form the fixed effect $\mathcal{A}_j(\mathbf{x}_i)$, along with posterior summaries of the associated “principal” functions

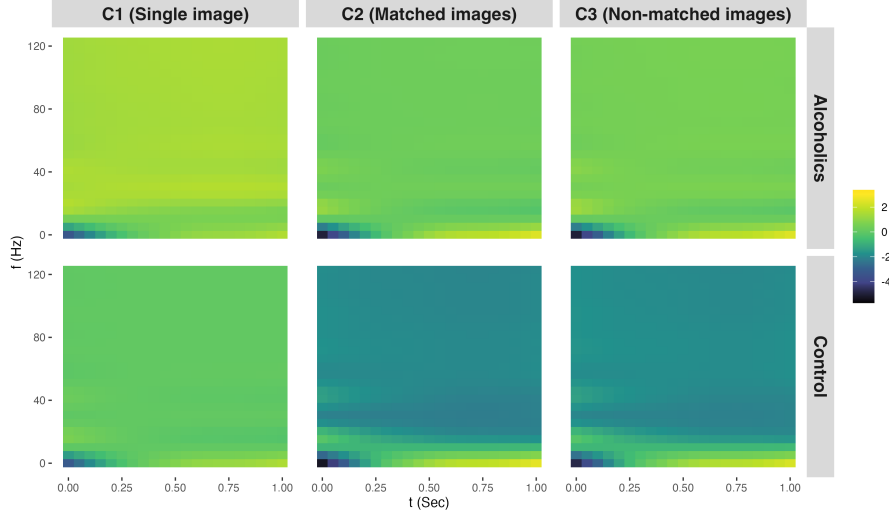


FIG 6. Posterior means of the stimulus condition- and group-specific fixed effect $A_j(\mathbf{x}_i)$ evaluated on a $t \times f$ grid, shown for combinations of conditions (C_1 , C_2 , C_3) and groups (Alcoholics vs. Control), highlighting differences across conditions and groups.

$\phi_r^*(t)$ and $\psi_r^*(f)$ and the covariate-modulated weights $\lambda_{j,r}(\mathbf{x}) = \delta_{j,r}^T \mathbf{x}$. In Figure 7, the Rank 1 “base” pattern primarily captures gamma-band (>30 Hz) activity with a modest increase over time, as reflected by the rising trend in $\phi_1(t)$ and elevated $\psi_1(f)$ values at high frequencies. The 95% credible intervals for the corresponding weights $\lambda_{j,1}(\mathbf{x})$ (the right-most column) indicate a significant difference between alcoholic and control groups under all conditions (C_1, C_2, C_3), suggesting that alcoholic subjects exhibit stronger gamma-band activity in response to the presentation of visual stimulus, compared to controls. This finding aligns with prior analyses of the same dataset under condition C_1 , which reported similar group difference in gamma-band activity (Bavkar, Iyer and Deosarkar, 2019; Qazi, Hussain and AboAlsamh, 2021). Our analysis extends these results by capturing both spectral and temporal dynamics and showing that the group gamma-band difference generalizes across all conditions, while also accounting for subject-specific neural responses unexplained by covariates. Moreover, we found that this group difference is more pronounced under conditions C_2 and C_3 , which involve more complex visual inputs (two images), compared to C_1 (a single image). The Rank 2 “base” pattern mainly reflects low-frequency activities (delta, theta and alpha bands; <12 Hz), with an increasing temporal trend. This trend aligns with established functional regulatory roles, where low-frequency oscillations are associated with functional inhibition (Bonnefond and Jensen, 2013), which tends to become more pronounced during post-stimulus transition towards the resting state. In addition, the weights $\lambda_{j,2}(\mathbf{x})$ differ significantly between condition C_1 and conditions C_2 and C_3 , but not between alcoholic and control groups (Figure 7, the right-most column). This implies that the Rank 2 pattern mainly captures condition-related effects, with C_2 and C_3 inducing stronger time-increasing low-frequency activities compared to C_1 .

5. Discussion. In this paper, we propose a Bayesian framework for modeling multilevel two-way functional data, motivated by analyzing time-frequency EEG responses collected under multiple experimental conditions. The proposed model incorporates fixed and random effects, capturing structured variability at the within-subject, between-subject, and between-condition levels, while accounting for the influence of covariates. Through a covariate-dependent CP decomposition, the proposed model enables estimation of the marginal contri-

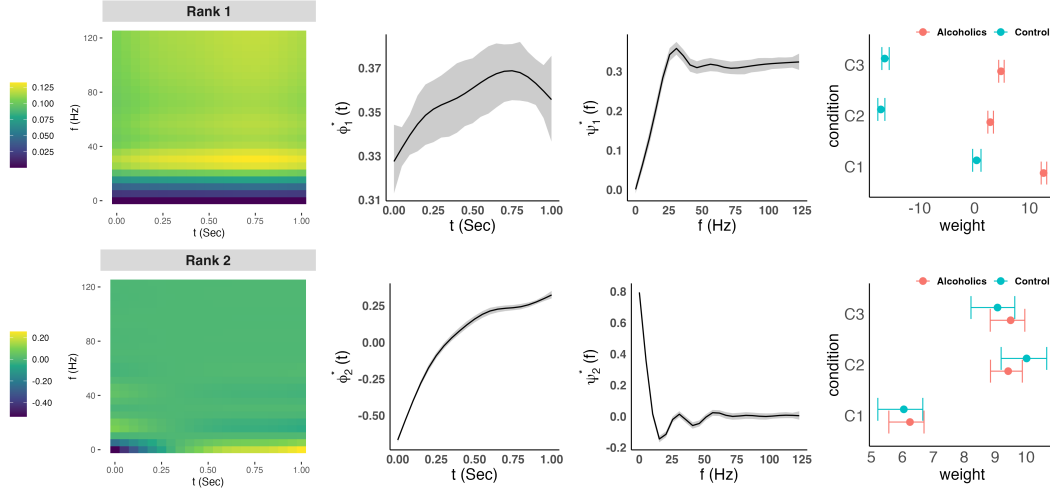


FIG 7. Visualization of rank-specific patterns and associated weights. Each row corresponds to a rank component ($r = 1$ and $r = 2$), and columns (from left to right) display: (1) posterior mean of the “base” pattern $\phi_r^*(t)\psi_r^*(f)$; (2) posterior mean and 95% credible interval of the time “principal” function $\phi_r^*(t)$; (3) posterior mean and 95% credible interval of the frequency “principal” function $\psi_r^*(f)$; and (4) 95% credible intervals of the weights $\lambda_{j,r}(\mathbf{x}) = \delta_{j,r}^T \mathbf{x}$, shown across combinations of conditions (C_1, C_2, C_3) and groups (Alcoholics vs. Control).

butions from time and frequency domains and efficiently captures interpretable latent structures (i.e., “base” patterns) shared across subjects and conditions. The Bayesian formulation, combined with the proposed posterior sampling algorithm and sparsity-inducing prior, provides an efficient approach for uncertainty quantification and CP rank selection. We demonstrated the advantages of our method in a simulation study, showing improved performance over existing approaches. In the EEG alcoholism case study, we found stronger gamma-band activity in alcoholic subjects relative to controls, along with differing levels of time-increasing low-frequency activity across stimulus conditions.

While this work focuses on time-frequency responses from a single region of interest, the proposed framework can be extended to multi-region data by generalizing the CP decomposition and tensor-product basis to higher-order tensors. Such an extension would allow for a more comprehensive characterization of spatial-temporal brain dynamics in the time-frequency domain, as well as providing a foundation for investigations into time- and frequency-resolved functional connectivity. Future work will also extend the framework to accommodate longitudinal EEG data collected over multiple visits.

Funding. The authors were supported by the National Institute of Health (NIH Grant No. 5 R01 MH099003).

SUPPLEMENTARY MATERIAL

Supplementary Material for “Bayesian Mixed-Effects Models for Multilevel Two-way Functional Data: Applications to EEG Experiments”

This file includes the identifiability proof, posterior derivations, additional results from the simulation studies, and code with usage instructions for **BMEF-1** and **BMEF-2**. It is available at <https://github.com/xmengju/BMEF>.

REFERENCES

ALAM, M. S., STAICU, A.-M. and SHI, P. (2024). Supervised low-rank approximation of high-dimensional multivariate functional data via tensor decomposition. *arXiv:2409.13819*.

- ALLEN, G. I. (2013). Multi-way functional principal components analysis. In *2013 5th IEEE International Workshop on Computational Advances in Multi-sensor Adaptive Processing (CAMSAP)* 220–223. IEEE.
- BAVKAR, S., IYER, B. and DEOSARKAR, S. (2019). Rapid screening of alcoholism: An EEG based optimal channel selection approach. *IEEE Access* **7** 99670–99682.
- BEGLEITER, H. (1995). EEG Database. UCI Machine Learning Repository. <https://doi.org/10.24432/C5TS3D>.
- BHATTACHARYA, A. and DUNSON, D. B. (2011). Sparse Bayesian infinite factor models. *Biometrika* **98** 291–306.
- BONNEFOND, M. and JENSEN, O. (2013). The role of gamma and alpha oscillations for blocking out distraction. *Commun. Integr. Biol.* **6** e22702.
- BORCHERS, H. W. (2022). *pracma: Practical Numerical Math Functions* R package version 2.4.2.
- CAMPOS, E. and SENTURK, D. (2025). *mhpca: Multilevel Hybrid Principal Components Analysis* R package version 1.0.0.
- CAMPOS, E., WOLFE SCHEFFLER, A., TELESKA, D., SUGAR, C., DISTEFANO, C., JESTE, S., LEVIN, A. R., NAPLES, A., WEBB, S. J., SHIC, F. et al. (2022). Multilevel hybrid principal components analysis for region-referenced functional electroencephalography data. *Stat. Med.* **41** 3737–3757.
- CAVANAGH, J. F. and FRANK, M. J. (2014). Frontal theta as a mechanism for cognitive control. *Trends Cogn. Sci.* **18** 414–421.
- CEDERBAUM, J., POUPLIER, M., HOOLE, P. and GREVEN, S. (2016). Functional linear mixed models for irregularly or sparsely sampled data. *Stat. Model.* **16** 67–88.
- CHEN, L.-H. and JIANG, C.-R. (2017). Multi-dimensional functional principal component analysis. *Stat. Comput.* **27** 1181–1192.
- CONG, F., LIN, Q.-H., KUANG, L.-D., GONG, X.-F., ASTIKAINEN, P. and RISTANIEMI, T. (2015). Tensor decomposition of EEG signals: a brief review. *J. Neurosci. Methods* **248** 59–69.
- CUI, E., LEROUX, A., SMIRNOVA, E. and CRAINICEANU, C. M. (2022). Fast univariate inference for longitudinal functional models. *J. Comput. Graph. Statist.* **31** 219–230.
- CUI, E., LI, R., CRAINICEANU, C. M. and XIAO, L. (2023). Fast multilevel functional principal component analysis. *J. Comput. Graph. Statist.* **32** 366–377.
- DI, C.-Z., CRAINICEANU, C. M., CAFFO, B. S. and PUNJABI, N. M. (2009). Multilevel functional principal component analysis. *Ann. Appl. Stat.* **3** 458–488.
- DONG, M., TELESKA, D., GUINDANI, M., SUGAR, C., WEBB, S. J., JESTE, S., DICKINSON, A., LEVIN, A. R., SHIC, F., NAPLES, A. et al. (2024). Modeling intra-individual inter-trial EEG response variability in autism. *Stat. Med.* **43** 3239–3263.
- GRAMFORT, A. and KOWALSKI, M. (2009). Improving M/EEG source localization with an inter-condition sparse prior. In *2009 IEEE International Symposium on Biomedical Imaging: From Nano to Macro* 141–144. IEEE.
- GREVEN, S., CRAINICEANU, C., CAFFO, B. and REICH, D. (2011). Longitudinal functional principal component analysis. In *Recent advances in functional data analysis and related topics* 149–154. Physica-Verlag, Heidelberg.
- GUO, W. (2002). Functional mixed effects models. *Biometrics* **58** 121–128.
- GYURKOVICS, M., CLEMENTS, G. M., LOW, K. A., FABIANI, M. and GRATTON, G. (2021). The impact of 1/f activity and baseline correction on the results and interpretation of time-frequency analyses of EEG/MEG data: A cautionary tale. *NeuroImage* **237** 118192.
- HAN, R., SHI, P. and ZHANG, A. R. (2024). Guaranteed functional tensor singular value decomposition. *J. Amer. Statist. Assoc.* **119** 995–1007.
- HAPP, C. and GREVEN, S. (2018). Multivariate functional principal component analysis for data observed on different (dimensional) domains. *J. Amer. Statist. Assoc.* **113** 649–659.
- HOFF, P. D. (2007). Model averaging and dimension selection for the singular value decomposition. *J. Amer. Statist. Assoc.* **102** 674–685.
- HOFF, P. D. (2009). Simulation of the matrix Bingham–von Mises–Fisher distribution, with applications to multivariate and relational data. *J. Comput. Graph. Statist.* **18** 438–456.
- HUANG, L., BAI, J., IVANESCU, A., HARRIS, T., MAURER, M., GREEN, P. and ZIPUNNIKOV, V. (2019). Multilevel matrix-variate analysis and its application to accelerometry-measured physical activity in clinical populations. *J. Amer. Statist. Assoc.* **114** 553–564.
- KENT, J. T., GANEIBER, A. M. and MARDIA, K. V. (2018). A new unified approach for the simulation of a wide class of directional distributions. *J. Comput. Graph. Statist.* **27** 291–301.
- KOLDA, T. G. and BADER, B. W. (2009). Tensor decompositions and applications. *SIAM Rev.* **51** 455–500.
- LI, Q., SHAMSHOIAN, J., ŞENTÜRK, D., SUGAR, C., JESTE, S., DISTEFANO, C. and TELESKA, D. (2020). Region-referenced spectral power dynamics of EEG signals: A hierarchical modeling approach. *Ann. Appl. Stat.* **14** 2053–2068.
- LOCK, E. F. and LI, G. (2018). Supervised multiway factorization. *Electron. J. Statist.* **12** 1150–1180.

- MALIK, A. S. and AMIN, H. U. (2017). *Designing EEG experiments for studying the brain: Design code and example datasets*. Academic Press, Cambridge, MA.
- MARQUAND, A. F., BRAMMER, M., WILLIAMS, S. C. and DOYLE, O. M. (2014). Bayesian multi-task learning for decoding multi-subject neuroimaging data. *NeuroImage* **92** 298–311.
- MEINARDI, V. B., LÓPEZ, J. M. D., FAJRELDINES, H. D., BOYALLIAN, C. and BALZARINI, M. (2024). Linear mixed-effect models for correlated response to process electroencephalogram recordings. *Cogn. Neurodyn.* **18** 1197–1207.
- MORALES, S. and BOWERS, M. E. (2022). Time-frequency analysis methods and their application in developmental EEG data. *Dev. Cogn. Neurosci.* **54** 101067.
- MORRIS, J. S. and CARROLL, R. J. (2006). Wavelet-based functional mixed models. *J. R. Stat. Soc. Ser. B* **68** 179–199.
- MORRIS, J. S., VANNUCCI, M., BROWN, P. J. and CARROLL, R. J. (2003). Wavelet-based nonparametric modeling of hierarchical functions in colon carcinogenesis. *J. Amer. Statist. Assoc.* **98** 573–583.
- PALMA, G. R., THORNBERRY, C., COMMINS, S. and MORAL, R. A. (2024). Understanding learning from EEG data: Combining machine learning and feature engineering based on hidden Markov models and mixed models. *Neuroinformatics* **22** 487–497.
- QAZI, E.-U.-H., HUSSAIN, M. and ABOALSAMH, H. A. (2021). Electroencephalogram (EEG) Brain Signals to Detect Alcoholism Based on Deep Learning. *Comput. Mater. Continua* **67** 3329–3348.
- RAMSAY, J. O. and SILVERMAN, B. W. (2005). *Functional Data Analysis*, 2nd ed. Springer, New York.
- RIHA, C., GÜNTENSBERGER, D., KLEINJUNG, T. and MEYER, M. (2020). Accounting for heterogeneity: mixed-effects models in resting-state EEG data in a sample of tinnitus sufferers. *Brain Topogr.* **33** 413–424.
- ROČKOVÁ, V. (2018). Bayesian estimation of sparse signals with a continuous spike-and-slab prior. *Ann. Statist.* **46** 401–437.
- SCHEIPL, F., GERTHEISS, J. and GREVEN, S. (2016). Generalized functional additive mixed models. *Electron. J. Statist.* **10** 1455–1492.
- SCHEIPL, F., STAIU, A.-M. and GREVEN, S. (2015). Functional additive mixed models. *J. Comput. Graph. Statist.* **24** 477–501.
- SHAMSHOIAN, J., SENTURK, D., JESTE, S. and TELESKA, D. (2020). LFBayes: Bayesian analysis of longitudinal and multidimensional functional data R package version 1.0.
- SHAMSHOIAN, J., ŞENTÜRK, D., JESTE, S. and TELESKA, D. (2022). Bayesian analysis of longitudinal and multidimensional functional data. *Biostatistics* **23** 558–573.
- SORT, L., BRUSQUET, L. L. and TENENHAUS, A. (2024). Latent functional PARAFAC for modeling multidimensional longitudinal data. *arXiv:2410.18696*.
- SPINNATO, J., ROUBAUD, M., BURLE, B. and TORRÉSANI, B. (2015). Detecting single-trial EEG evoked potential using a wavelet domain linear mixed model: application to error potentials classification. *J. Neural Eng.* **12** 036013.
- STEWART, G. W. (1973). *Introduction to matrix computations*. Academic Press, New York.
- STEWART, G. W. (1980). The efficient generation of random orthogonal matrices with an application to condition estimators. *SIAM J. Numer. Anal.* **17** 403–409.
- J. SUEUR, T. AUBIN and C. SIMONIS (2008). Seewave: a free modular tool for sound analysis and synthesis. *Bioacoustics* **18** 213–226.
- SUN, T. (2023). FLFOSR: Fast Longitudinal Function-on-scalar Regression R package version 0.0.0.9000.
- SUN, T. Y. and KOWAL, D. R. (2025). Ultra-efficient MCMC for Bayesian longitudinal functional data analysis. *J. Comput. Graph. Statist.* **34** 34–46.
- TANG, X., BI, X. and QU, A. (2020). Individualized multilayer tensor learning with an application in imaging analysis. *J. Amer. Statist. Assoc.* **115** 836–851.
- VEHTARI, A., GELMAN, A. and GABRY, J. (2017). Practical Bayesian model evaluation using leave-one-out cross-validation and WAIC. *Stat. Comput.* **27** 1413–1432.
- VOLKMANN, A., STÖCKER, A., SCHEIPL, F. and GREVEN, S. (2023). Multivariate functional additive mixed models. *Stat. Model.* **23** 303–326.
- WU, W., WU, C., GAO, S., LIU, B., LI, Y. and GAO, X. (2014). Bayesian estimation of ERP components from multicondition and multichannel EEG. *NeuroImage* **88** 319–339.
- ZHANG, X. L., BEGLEITER, H., PORJESZ, B., WANG, W. and LITKE, A. (1995). Event related potentials during object recognition tasks. *Brain Res. Bull.* **38** 531–538.
- ZHANG, J., SIEGLE, G. J., SUN, T., D’ANDREA, W. and KRAFTY, R. T. (2023). Interpretable principal component analysis for multilevel multivariate functional data. *Biostatistics* **24** 227–243.
- ZIPUNNIKOV, V., GREVEN, S., SHOU, H., CAFFO, B., REICH, D. S. and CRAINICEANU, C. (2014). Longitudinal high-dimensional principal components analysis with application to diffusion tensor imaging of multiple sclerosis. *Ann. Appl. Stat.* **8** 2175–2202.